



저작자표시-비영리-변경금지 2.0 대한민국

이용자는 아래의 조건을 따르는 경우에 한하여 자유롭게

- 이 저작물을 복제, 배포, 전송, 전시, 공연 및 방송할 수 있습니다.

다음과 같은 조건을 따라야 합니다:



저작자표시. 귀하는 원저작자를 표시하여야 합니다.



비영리. 귀하는 이 저작물을 영리 목적으로 이용할 수 없습니다.



변경금지. 귀하는 이 저작물을 개작, 변형 또는 가공할 수 없습니다.

- 귀하는, 이 저작물의 재이용이나 배포의 경우, 이 저작물에 적용된 이용허락조건을 명확하게 나타내어야 합니다.
- 저작권자로부터 별도의 허가를 받으면 이러한 조건들은 적용되지 않습니다.

저작권법에 따른 이용자의 권리는 위의 내용에 의하여 영향을 받지 않습니다.

이것은 [이용허락규약\(Legal Code\)](#)을 이해하기 쉽게 요약한 것입니다.

[Disclaimer](#)

이학박사 학위논문

Telegraph Noise of Domain Wall Dynamics

자구벽 동역학의 텔레그래프 노이즈

2022년 6월

서울대학교 대학원

물리천문학부

전 세 영

Telegraph Noise of Domain Wall Dynamics

자구벽 동역학의 텔레그래프 노이즈

지도교수 최석봉

이 논문을 이학박사 학위논문으로 제출함

2022년 6월

서울대학교 대학원

물리천문학부

전 세 영

전세영의 이학박사 학위논문을 인준함

2022년 6월

위 원 장 김 창 영 (인)

부위원장 최 석 봉 (인)

위 원 민 홍 기 (인)

위 원 양 범 정 (인)

위 원 김 지 완 (인)

Telegraph Noise of Domain Wall Dynamics

Seyyoung Jeon

Supervised by
Professor Sug-Bong Choe

A Dissertation in Physics

Submitted to the Faculties of
Seoul National University
in Partial Fulfillment of the Requirements for the Degree of
Doctor of Philosophy

June 2022

*Department of Physics and Astronomy
The Graduate College of Natural Sciences
Seoul National University*

Abstract

In modern society, a lot of information, especially first-class personal information such as account numbers, is digitalized and converted into data. Accordingly, interest in data encryption has emerged. Often, a lot of data can be encrypted with a computer algorithm, but these commonly require an original input value, that is, a 'seed number'. Because the seed number should be unpredictable, it is inevitable to exclude the software algorithm. So, a random number using hardware such as rolling a dice or tossing a coin is required. Device implementation of those things is called true random number generator or hardware random number generator.

In order to design a true random number generator, it is important to choose the source of the random number. Studies on true random number generators focus on finding and applying those sources that are appropriate for a good random number generator. One of candidates is telegraph noise which resembles two-level digital bits. This thesis is dedicated to understanding the telegraph noise of magnetic domain wall motion and testing for device applications utilizing the understanding of the energy barrier of magnetic

domain wall.

It is the first step to develop the measurement system and to fabricate appropriate samples. Microscope specialized in detecting telegraph noise was developed and sample was chosen for field and current-induced domain wall motion. A method to measure the telegraph noise was established for controllable and repeatable measurements of domain wall depinning phenomena. Other appendices to measurement are also presented.

Then, the experiment for understanding the energy barrier of magnetic domain wall in different magnetic fields and electric current conditions was conducted to study the relation between the energy barrier and these external inputs. Some of the physical origins were found through derivation of the energy barrier.

Next, Arrhenius law of activation was confirmed. Setup for temperature experiment was designed suitable for the temperature variation. Temperature dependence of statistics of telegraph noise verified the activation law of overcoming energy barrier.

Finally, the random numbers of domain wall telegraph noise were tested. Basic tests such as probability and autocorrelation of the bits were carried out and appropriate field and current conditions for true random bits are found. In combination with the understanding of energy barrier, conditions for an unpredictable and fast random number generator were proposed.

These research to understand and test the telegraph noise can be starting point to develop the true random number generator based on magnetic

domain wall, which is an exclusive form of telegraph noise source other than FET, memristor, or magnetic tunnel junction.

Keywords: Telegraph noise, magnetic domain wall, domain wall motion, domain wall pinning, energy barrier, Arrhenius law, cryptography, true random number generator, hypothesis test, spin-orbit torque, perpendicular magnetic anisotropy

Student number: 2013-20381

Table of Contents

Abstract	i
List of Figures	vi
List of Tables	viii
1 Introduction	1
2 Measurement system and sample fabrication.....	6
2.1 Measurement system	8
2.2 Sample preparation	21
2.3 Process for measuring telegraph noise.....	25
3 Depinning energy barrier of domain wall.....	29
3.1 Introduction.....	31
3.2 Energy barrier E_B of telegraph noise	31
3.3 Dependence of energy barrier E_B on field H and current J	41
3.4 Summary of chapter 3	53
4 Verification of Arrhenius law.....	54
4.1 Add-on setup for temperature experiment	55
4.2 Result and discussion.....	60
5 Randomness of telegraph noise	63
5.1 Test method.....	64

5.2 Probability of telegraph noise	70
5.3 Autocorrelation of telegraph noise	74
5.4 Summary with comments on device application	78
6 Conclusion	82
References.....	84
Abstract in Korean	90
Author's Biography	93
Publications	94

List of Figures

Figure 1	Examples of telegraph noise in various system.....	11
Figure 2.1	Diagram of measurement setup.	18
Figure 2.2	Outlook of laser section.....	20
Figure 2.3	Outlook of MOKE microscope	22
Figure 2.4	Magnetic field loop of Pt/Co($t=1.0$ nm)/W thin film.	23
Figure 2.5	Images of domain wall scanning.....	26
Figure 2.6	Calculation of domain wall signal	29
Figure 2.7	Images of magnetic film.....	31
Figure 2.8	Images of the fabricated nanowire structure	33
Figure 2.9	Schematics of measuring telegraph noise.....	36
Figure 2.10	Process of telegraph noise to depinning time.....	38
Figure 3.1	Microscope image of experimental spot.....	44
Figure 3.2	Example measurement for the statistic research.....	47
Figure 3.3	$1 - F(t_d^-)$ of telegraph noise	49
Figure 3.4	$1 - F(t_d^-)$ in several current conditions.....	53
Figure 3.5	E_B^\pm in various applied field and current	55
Figure 3.6	Plots fitting results of figure 3.5	56
Figure 3.7	Energy landscape of telegraph noise site.....	59
Figure 4.1	Outlook of add-on setup for temperature experiment	65
Figure 4.2	Test result of temperature measurement	67
Figure 4.3	Result of temperature experiment.....	70
Figure 5.1	Conceptual description of hypothesis test	77
Figure 5.2	Controllability test result of P	80

Figure 5.3 Randomness test of \mathbf{P}	81
Figure 5.4 Properties of $\mathbf{R}_{xx}(l)$ with respect to the sampling time t_s	84
Figure 5.5 Controllability test result of \mathbf{R}_L	86

List of Tables

Table I Extracted values of E_0 , a , ε	55
Table II Displacement to the saddle point from each pinning sites	59

Chapter 1

Introduction

Noise is considered an undesirable phenomenon in scientific research and effort has been made substantially to minimize or circumvent these unwanted effects when developing experimental setup. As the modern scientific projects evolved to acquire much minute signal, several efforts have also been made to understand the noise, especially the electrical noise of semiconductors, because in modern scientific research, signals of many kinds are transduced in the form of electricity by using semiconductor devices. Those studies categorize the electrical noise into several different types such as flicker noise, thermal noise, shot noise, etc. [1], some of which shows so intriguing behavior that it is sometimes called as ‘signal’, not just as ‘noise’, like telegraph noise [2].

Telegraph noise is a type of noise the waveform of which transits between certain limited levels as random. Owing to its discrete feature that appears as on-off signals of traditional electronic telegraph communication, it is also called burst noise or popcorn noise [2–4]. Although it was mainly considered original character of semiconductor such as field-effect transistor (FET) [5], it has recently been reported in the other systems like memristor [6], magnetic-tunnel-junction (MTJ) [7], and magnetic domain wall [8]. The reason

why that peculiar phenomenon arises in the different systems is attributed to its generation mechanism related to the energy barrier of the systems. It takes place in the systems that maintain continuous transitions between two (or more) metastable states that are energetically proximate. Metastable states are occupied alternately over time, either by thermal activation or with the aid of other system inputs (usually currents), the pattern of which appears random. Trapping/detrapping of single charge carrier in FET [9], up/down reversal of magnetization in MTJ [10], or pinning/depinning of magnetic domain wall at adjacent pinning sites [8] can be examples of metastable states pair that generate telegraph noise.

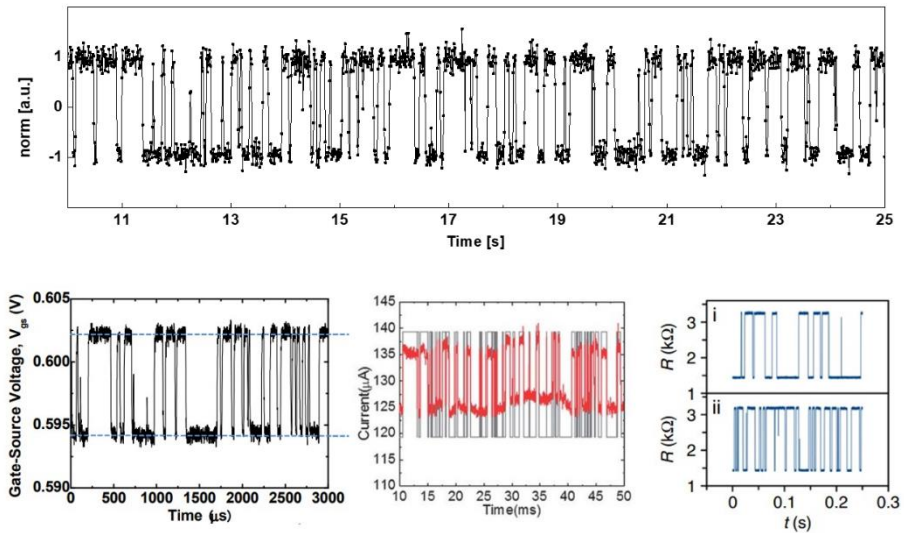


Figure 1 Examples of telegraph noise in various systems. Upper figure is the example of telegraph noise from the domain wall motion which is normalized with the base level signal drift. Lower figure sets are from the left side the example of telegraph noise by, 1) field-effect transistor [5], 2) memristor [6], 3) magnetic-tunnel junction [7].

Telegraph noise, with its discrete nature, has recently been highlighted in cryptography for its potential to implement a true random number generator (TRNG), which is a key to secure data encryption [11]. A TRNG, as the name suggests, must generate ‘truly random numbers’, which is totally different from the pseudorandom number generator (PRNG), where the random number is generated by algorithm the seed numbers of which is created by TRNG. It is also known as hardware random number generator (HRNG) as it exploits natural entropy sources that appeared to be unpredictable such as coin flip/flop, rolling dice, or white noise of electric circuit [12]. As the fact that the telegraph noise itself can be a 2-bit digital signal, several studies have attempted to exploit the potential of telegraph noise to develop TRNG, mainly in the system based on FET [13] or MTJ [14]. These studies have focused on manipulating the energy barrier that generates telegraph noise [14] because the energy landscape governs the probability of up/down bit occurrence and rate of bits transition, which is key factor of realizing high speed TRNG of high unpredictability. So, it is important to understand the physical characteristics of energy landscape of these metastable states.

This energy barrier, which is also present in domain wall dynamics, is a major cause of domain wall pinning/depinning. The study of domain wall depinning dynamics has been one of the main topics of magnetic domain wall dynamics in that it determines stabilities and power efficiency of devices based on racetrack model [15]. Most of the experiments performed in these studies

are to estimate domain wall energy barrier by measuring domain wall depinning times of pinning site [16–18]. Since the magnetization reversal process by the domain wall motion is generally irreversible, it is essential to retract or rewrite the domain wall at specific pinning sites in order to repeat measurement, which requires excessive time and accompanies application of extra current and/or magnetic field. Contrary to the process above, the pinning/depinning of the domain wall in the telegraph noise process occurs reproducibly and repeatedly, resulting in rapid data acquisition for two (or more) pinning sites simultaneously. Recently, S.-J. Yun et al [19] investigated the telegraph noise on a single energy barrier for current-pulse driven domain-wall depinning. In this thesis work, the previous work is extended for the double energy barrier of two pinning sites under more general condition of DC current and magnetic field, which complete the domain wall dynamics of telegraph noise. The relation between energy barrier and experimental inputs has been found and physical meaning of the parameters of the relationship is analyzed by accompanying energy barrier theory [20].

Applicability of telegraph noise generated by domain wall motion is investigated by testing primary characteristics of random numbers sampled by the raw data. To determine whether a sequence of numbers is random is a lot more complicated than we thought. However, for 2-bit case, one might intuitively think that random bits should be generated equally and the bit after a certain bit should be unpredictable, which can be rephrased as probabilities

and autocorrelation of bits. In this paper, two characteristics of randomness are reviewed to determine the possibility of a new type of TRNG at the basic stage. It is investigated how the two characteristics change and which condition makes bits random under condition of applied current or field. Then the testing results are combined with the study of energy barrier of pinning sites and the best feature of energy landscapes for TRNG are determined.

The contents of the thesis work are as follow. After this introduction, setup for telegraph noise measurement is presented in **Chapter 2** including the sample preparation. Energy landscape of pinning sites that generate telegraph noise is examined in **Chapter 3** by considering the effect of electric current and magnetic field. To confirm the analysis of previous chapter, Arrhenius law governing the rate of overcoming energy barrier is verified by add-on setup for temperature experiment in **Chapter 4**. Then, **Chapter 5** tests the basic randomness of the bits extracted from telegraph noise and examines the relationship between the true random bits and the energy landscape. The results are summarized in **Chapter 6**.

Chapter 2

Measurement system and sample fabrication

In order to measure the telegraph noise of domain wall motion, there is utmost important factor to be considered, no matter which method is used for the magnetic signal measurement, e.g., optical [21], magnetoresistance [22], or hall-bar method [23]. Spatial resolution of the measurement system is a key factor in determining the signal level of telegraph noise, since the magnitude of phenomena is sub-micron [8,19]. In this thesis work, telegraph noise was measured by optical microscope using magneto-optic Kerr effect (MOKE). Components that determine the spatial resolution of microscope are investigated and the results are applied to obtain better resolution. Besides the spatial resolution, other components that conclude the system are decided in order to obtain better signal. It is presented in **Section 2.1** how the measurement system is designed to carry out telegraph noise research.

Sample fabrication is also prepared with care to optimize the measurement under various conditions. Magnetic thin film is chosen in which the domain wall moves well in magnetic field and electric current condition and the signal levels are maximized for the probe beam wavelength. Structure of the sample is designed considering experimental and application suitability. In

Section 2.2, essential samples designed and used for the experiment are presented.

Experimental method details are presented in **Section 2.3** which include the domain wall writing methods using the power of probe laser beam. Shutter arrangements are devised for program-controllable experiment. Experimental flow is also explained and tips for conducting the measurement repeatedly under the same condition are presented.

2.1 Measurement System

System can be separated conceptually and spatially into two sections. One is the laser section which consists of a laser source, a second-harmonic generation part, an intensity control shutter, and a delay stage. The other is microscope section, the arrangement of which configures a general MOKE microscope containing polarizer and analyzer with some differences in detail. Sample are placed in sample stage which is designed to be able to experiment with different magnetic field and electric current. All optical components are installed on the optical table (M-ST-48-12, Newport) and floated by isolators using air compressor to keep the measurement system away from the various noises on the ground. Concept diagram of the system is presented in figure 2.1.

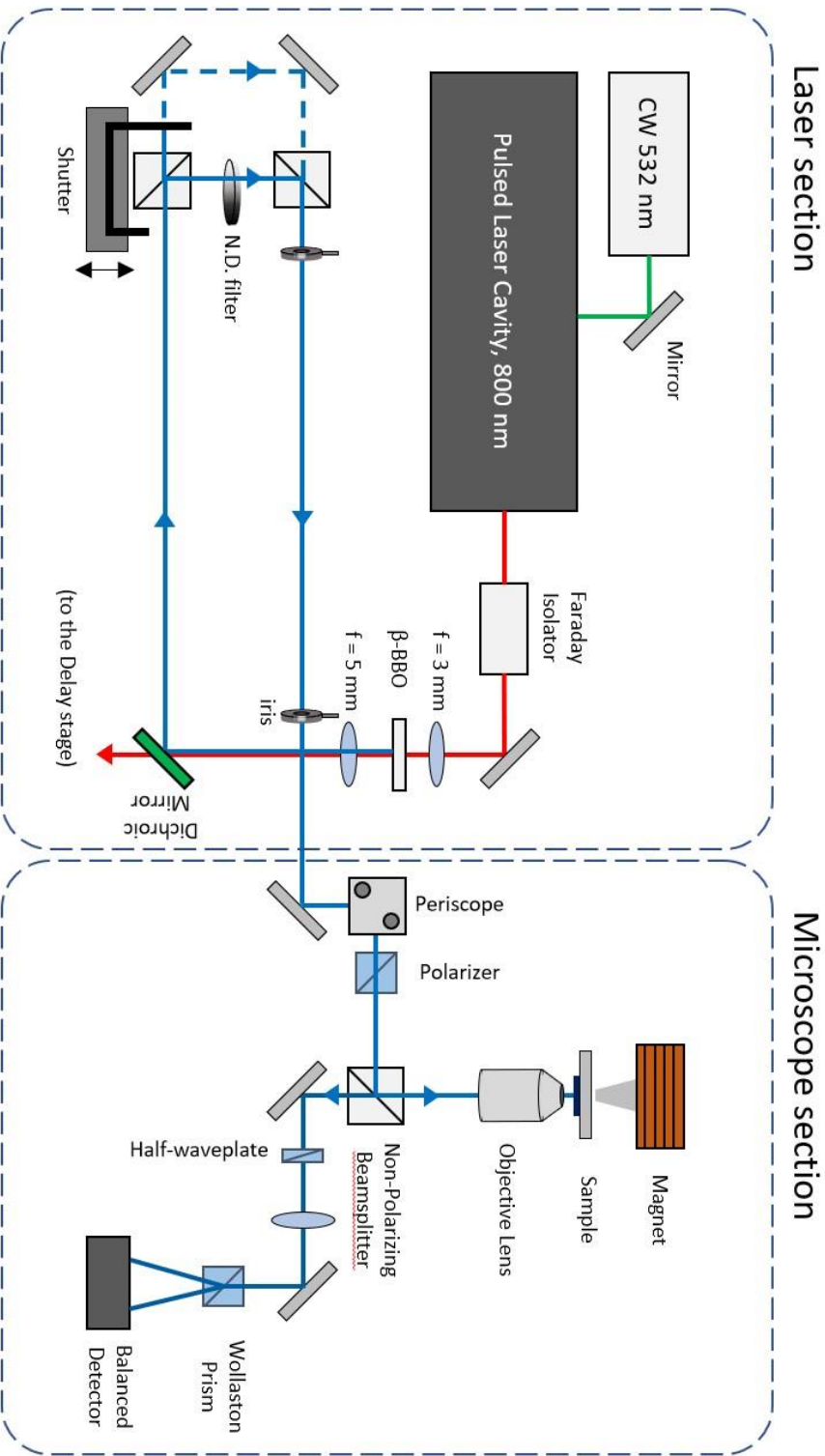


Figure 2.1 Diagram of measurement setup

2.1.1 Laser section

This microscope system is operated by pulsed laser. Seed laser (Millennia eV5, Spectra-Physics) of the pulsed laser is diode-pumped solid state continuous laser of 4.5 W in power, 532 nm in wavelength and p-polarization (pol). This laser emits beam of 1mm in diameter onto a 532 nm V-coated mirror which guides the beam into the pulsed laser cavity. Pulsed laser cavity (MTS Laser, KMLabs) glows broad band 800 nm light from the Ti:Sapphire crystal excited by the seed beam and the light is aligned parallel by the two concave mirror, which makes continuous laser state. By triggering motion, the continuous laser is converted into pulsed laser based on the Kerr-lens mode locking of the Ti:Sapphire crystal, whose the pulse width is 100 fs and repetition rate is 93.7 MHz. Pulsed laser emitted from the cavity is p-polarized and converted into s-pol after the beam passes through the Faraday isolator. Then the 800 nm beam is focused on the beta-barium borate crystal (EKSMA optics) by $f = 3$ mm achromatic lens to generate frequency-doubled, 400 nm beam of p-pol by second harmonic generation. The maximum ~ 30 mW beam is converted from the 800 nm beam of ~ 500 W, which is measured right after the cavity, and the beams of two color are then collimated into parallel rays by $f = 5$ mm achromatic lens and are split by the dichroic mirror. The 800 nm beam is used as pump beam of photoconductive switch for the ns pulsed-current experiment or can be used as a pump source of pump-probe

measurement after passing delay stage. The 400 nm beam is reflected from the dichroic mirror and enter the shutter stage which controls intensity of the beam to the microscope section. The output beam of different power is selected by the positions of the shutter, which determines the function of 400 nm beam. Detailed structure and function of shutter stage is described in the experimental method part. The beam exits from the shutter stage and enters the microscope section through the long passage which is aligned by two irises at each end of passage. The description above can also be checked with the figure 2.2.

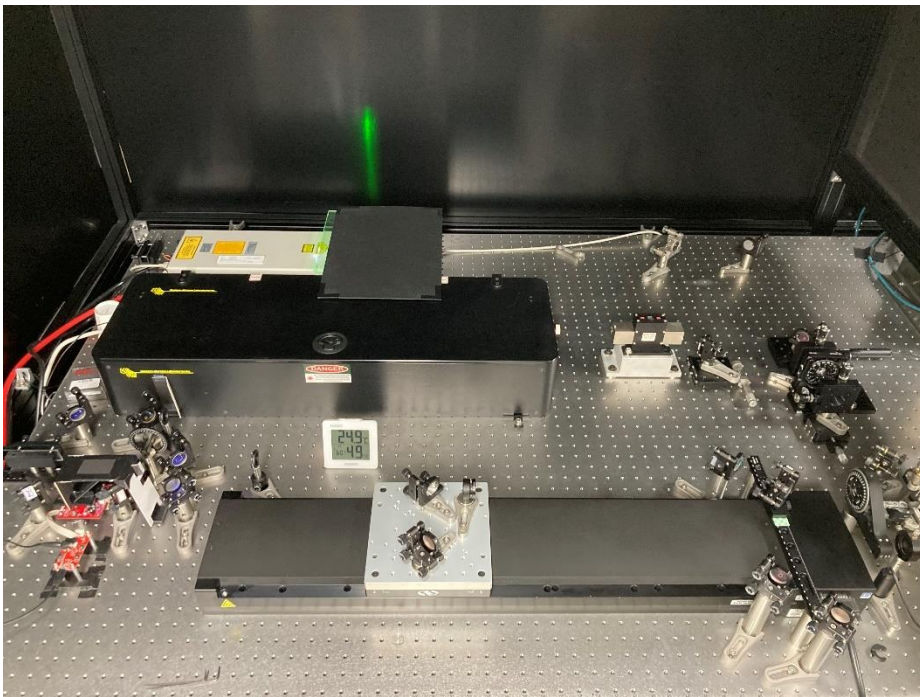


Figure 2.2 Outlook of Laser section

2.1.2 Microscope section

Laser beam of 400 nm wavelength and p-pol incidents into the microscope part, which is converted into s-pol with high extinction ratio ($\sim 1:100,000$, referring to the spec. sheet) after passing periscope and then Glan-Laser calcite polarizer (GL10-A, Thorlabs). Then the beam progresses to the non-polarizing beamsplitter with high transmittance (BSF10-A, Thorlabs) and then is reflected to the objective lens (TU Plan Fluor 100X, Nikon) which is right before the sample. Direction of incident beam and the sample normal is parallel, constituting the p-MOKE arrangement. In other words, the microscope measures magnetizations perpendicular to the sample, hence the main target of measurement is magnetic thin film with perpendicular magnetic anisotropy. While the beam focused onto and then reflected from the sample, its polarization is slightly rotated by the MOKE. Most of the reflected beam from the sample passes through the non-polarizing beamsplitter and then enters the analyzer part of MOKE microscope. A zero-order half-wave plate (10RP02-48, Newport) rotates the polarization by 45° and a plano-convex lens focuses the beam by the size less of detector's diode. Since the balanced detector (PDB450A, Thorlabs) is used, the beam of 45° polarization is separated into p- and s-pol components by a Wollaston prism (WP10-A, Thorlabs) before reaching the detector. The intensities of the separated beams are almost the same and differ only by the MOKE angle by the magnetization

of the sample. So, the balanced signal of the two beam yields the magnetization information of the samples, the common beam intensity fluctuations being compensated.

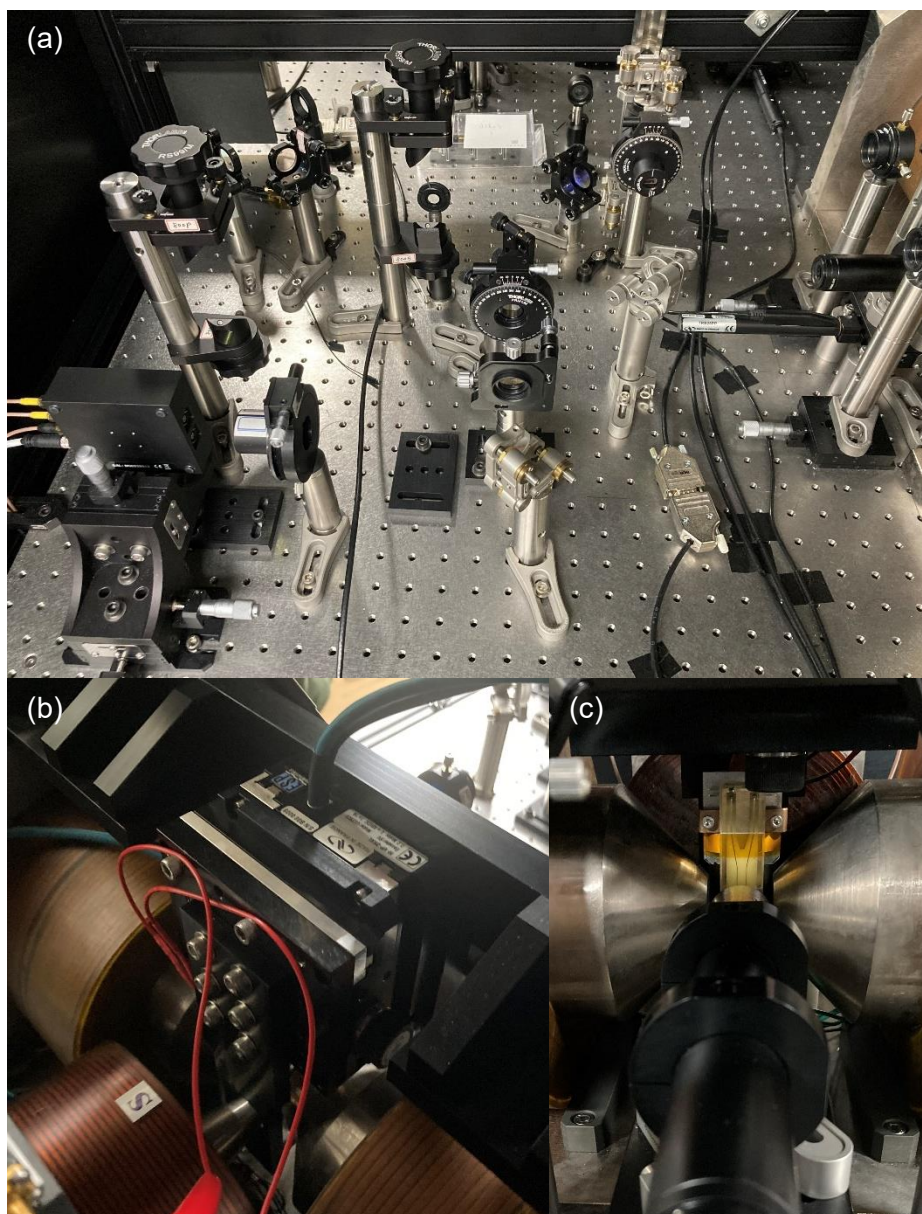


Figure 2.3 Outlook of MOKE microscope. (a) Optical components for polarizer and analyzer. (b) Electromagnet and sample stage which is behind the sample surface. (c) Front view of the objective lens and sample holder.

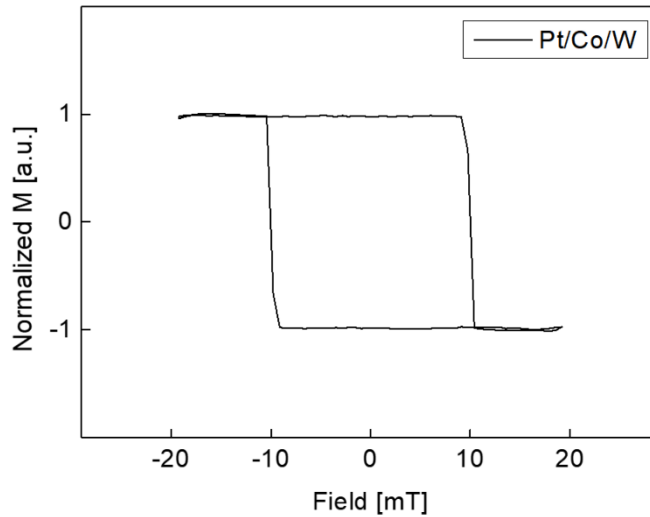


Figure 2.4 Magnetic field loop of Pt/Co ($t=1.0$ nm)/W thin film. The signal is measured by MOKE microscope and normalized according to the magnetization of the film.

The sample stage is equipped with two motorized linear stage (VP25-XL, Newport) each of which determines the positions of the sample with respect to the focused beam position in x, y plane, controlled by PC-based motion controller (XPS-Q8, Newport). Nanometer scale scanning is available with the 10 nm minimum incremental motion (MIM) of the linear stage and the travel range is up to ± 25 mm. The objective lens is installed on a linear stage equipped with a motorized actuator (TRB25PP, Newport), controlled by the same controller same as the sample stage, MIM of which is 100 nm sufficient for fine focusing.

Here is explained the effort to improve signal-to-noise ratio (SNR) by some explanations for choosing each component. This microscope has much lower power limit of incident beam for sample damaging ($< \sim 1 \text{ mW}$) compared to its available power range ($< \sim 30 \text{ mW}$). Possible explanations of that problem are as follow: high flux of focused beam resulting from high numerical aperture of object lens combined with low beam wavelength. This results in damage on sample by the beam power over approximately $\sim 1 \text{ mW}$ (measured right before the objective lens). This harsh limitation of beam power inevitably leads to lower beam intensity at the detector, and hence poor SNR. To improve the SNR in this setup, it is crucial to preserve the power of the beam reflected from the sample as much as possible. That is, core beamsplitter should have high transmittance (T) and low reflectance (R), so the beam sampler of $R : T = 5 : 95$ is selected for that reason. Furthermore, according to the datasheet of the beam sampler showing typical R (and T) curves over incident angles, the beam whose polarization is parallel to the plane composed by wavevector and reflection surface normal, has higher transmittance than the beam whose polarization is perpendicular to the plane. The former polarization corresponds to p-pol and the latter one does to s-pol. When the incident beam is s-pol, the MOKE component becomes p-pol in which the information of the magnetization is conserved at max.

2.1.3 Spatial resolution and signal estimation

Spatial resolution of the system can be checked by scanning edge of structure whose step is much smaller than the diameter of the focused beam. According to the specification of the setup, where the wavelength is 400 nm and numerical aperture of objective lens is 0.9, expected diameter of the perfectly focused beam is $d = 1.22 \lambda / \text{N.A.} = 542 \text{ nm}$. This length is much larger than the step size of structure fabricated by e-beam lithography. Another example of nanometer-scale step is, for the MOKE microscope, the magnetic domain wall. It is not a real structure, but a magnetic transition in space from up-domain to down-domain, the MOKE signal of which results in a step. Although width of domain wall varies with respect to the samples of different compositions, sample of long wall width reaches $\sim 40 \text{ nm}$ (e.g., Permalloy [15]) and it can be estimated that the magnetic film with high anisotropy has much shorter wall width of few nm. Therefore, it is possible to obtain a ‘magnetic’ spatial resolution straightforwardly by scanning magnetic domain wall.

Scanning microscope images

Images of the sample are obtained by scanning an area using probe beam. Figure 2.5 shows the images of structures captured by this experimental setup. Figure 2.5 (a) is the scanning image of nanowire captured by the signal proportional to the full intensity of the beam. Figure 2.5 (b) is obtained from

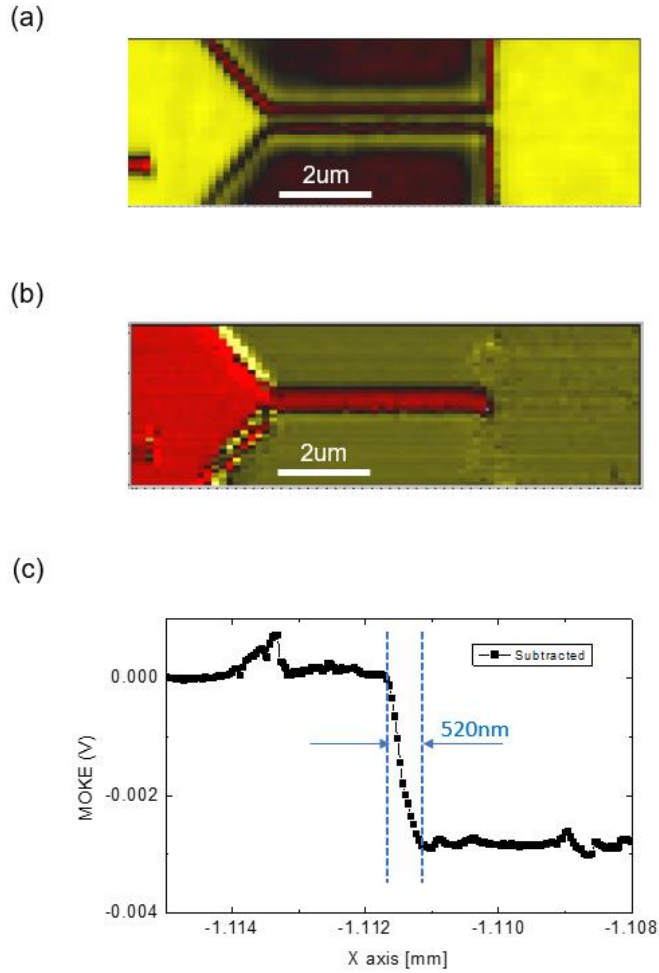


Figure 2.5 Images of domain wall scanning (a) 2-D image of 500 nm nano wire captured by scanning microscope (b) 2-D image of domain wall in the same window of (a). (c) Line scans of domain wall.

the signal proportional to the MOKE by subtracting the image after the domain wall writing to the image before domain wall writing where all the magnetization of the sample is down-saturated. Hence the image shows the contrast of the up-domain with respect to down-domain and substrate. As red color representing up-domain, it is clearly shown in the images that the up-

domain propagates through the nanowire of width 500 nm, and then positions at the exit of the wire. Because, in the image obtained by subtracting each image of the same window, the structure and magnetic domain are sharply cut and clearly deterministic, it is evident that the scanning system is not only stable but also repeatable with high spatial resolution.

Figure 2.5 (c) is 1-dimensional line scan of the up/down-domains with respect to x-axis by step size 40 nm. The line is expected to take form of an error function by analytic calculation, when the profile of the focused beam takes gaussian function and it scans over the edge of Heaviside function. The line scan shows clear error function profile which falls over 520 nm, indicating that the diameter of the focused beam would be sub-um and it is available to measure the signal of the domain wall motion of 40 nm or less. With the small displacement of domain wall X at the center of focused beam, it expected that the signal differences by the displacement is given by the ratio with respect to the full up/down signal (I_{FM}) as follows.

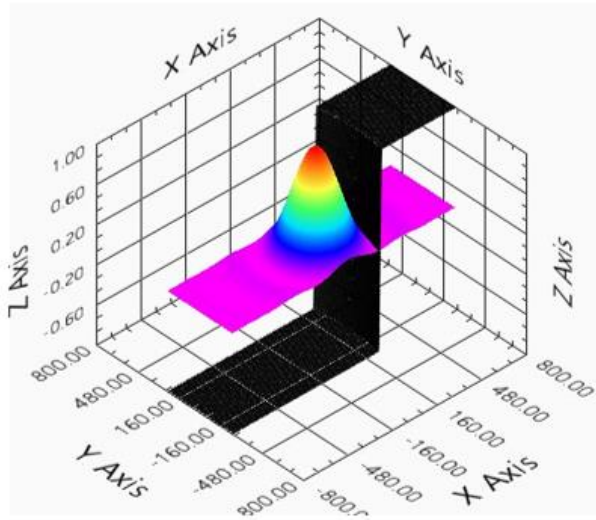
$$r = \frac{I_{TN}}{I_{FM}} = \sqrt{\frac{2X}{\pi\sigma}}, \quad (X \ll \sigma) \quad (1)$$

Here, the σ is full width of half maximum (FWHM) of the focused beam assumed to be gaussian. Equation (1) can be the measure of the telegraph noise level when the beam is focused on the maximum signal spot, in other words, the center of X .

Computation of telegraph noise signal

Signal level of telegraph noise is calculated numerically by the program. Figure 2.6 (a) shows the schematic image of calculation done by LabVIEW. Colored surface is the waveform of the focused beam, which is normalized airy function of peak intensity 1. Black one is the waveform of the magnetic domain the up/down magnetizations of which is valued to 1/-1. The calculated MOKE signal is the pixel-by-pixel summation, the product of beam signal times magnetic domain values of 1/-1. Size of a pixel is set to $2 \times 2 \mu\text{m}^2$. Wire structure is assumed to be 500 nm wide. Figure 2.6 (b) shows the result of the calculation. Black line is the percentage of telegraph noise level with respect to the up/down signal (or it can be called full MOKE signal as it is maximum value of the magnetic domain measurement). It is obtained by subtracting each result of the distanced domain walls. Red and green line is the results obtained by each domain wall that are distanced parallelly by 20nm. As the full MOKE value is 2 in this calculation, telegraph noise level is calculated by subtracting green from red line and normalized by 2. Result (black line) shows that up to 8.5 % of full MOKE is expected by telegraph noise when it is generated by the parallel motion alternating the two pinning sites 20 nm apart.

(a)



(b)

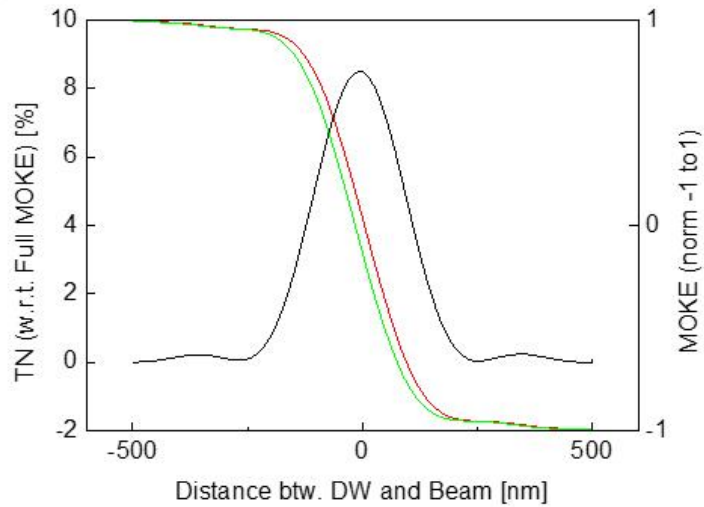


Figure 2.6 Calculation of domain wall signal (a) 3-dimensional visualization of focused beam (rainbow) and domain walls (black). (b) Calculated level of telegraph noise (black, left scale) and domain wall (color, right scale) with respect to the distance between domain wall and beam center.

2.2 Sample preparation

2.2.1 Film deposition

Sample was selected to have clear domain wall that move easily by the applied electric current. Recently, it has been studied extensively about the magnetic films of Pt/Co/W, which shows properties profit to this experiment [24,25]. It shows high speed current-induced domain wall motion at zero magnetic field. Plus, it shows high endurance in joule hitting which is useful for high current pulse experiment. Magnetic film is deposited by DC sputtering in ultrahigh vacuum chamber. Base pressure of the chamber is

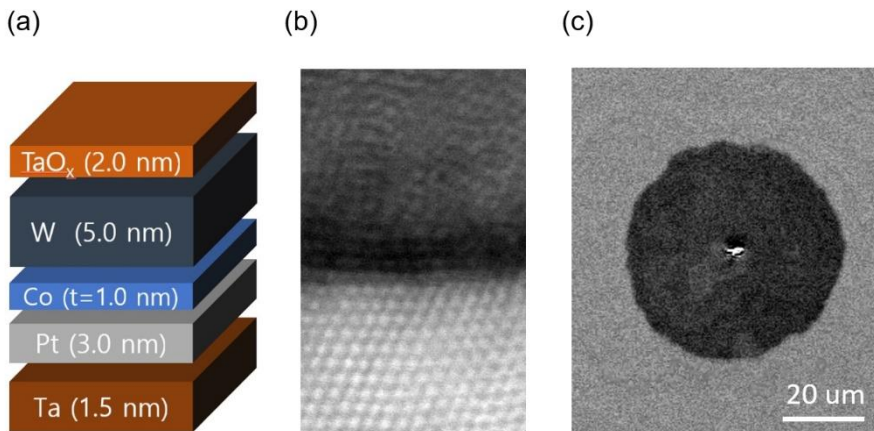


Figure 2.7 Images of magnetic thin film. (a) Deposition of the samples on the Si/SiO_x substrate, thickness of the sample measured are 0.9, 1.0 nm. (b) Cs-STEM image of the film. Black narrow layer in the middle indicates cobalt layer. (c) Full-field MOKE microscope image of circular magnetic domain. Distinct contrast indicates up/down magnetic domain.

below 1.0×10^{-8} Torr. For the case of the Pt/Co (0.7)/W film, the Cs-STEM image is obtained at National Center for Inter-University Research Facilities in the university. As shown in figure 2.7 (b), cobalt layer of 0.7 nm can be distinguished clearly, revealing 3 – 4 discrete monolayers.

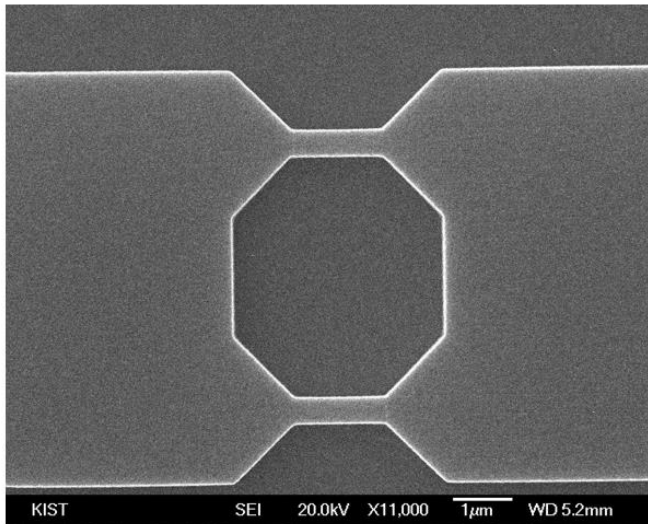
2.2.1 Structure fabrication

Nanostructures are advantageous for telegraph noise measurement for several reasons. In measurement aspects, the smaller the width of wire is, the easier it is to constrain the displacement variation of the domain wall. When domain wall is propagated from nucleation point by the field, it is natural for domain wall to be shaped round. To find the telegraph noise site by scanning MOKE, domain wall should be traced by probe beam while checking for the noise. It is harder to trace round wall than to trace flat wall. Moreover, since telegraph noise site appears in low probabilities, the uncertainty of domain wall position even worse the finding telegraph noise site. Therefore, to increase the possibilities of finding the site within the secured domain wall positions, narrow nanowire of width 500 – 200 nm (less than the diameter of the focused beam) is designed and the 2, 3 copies of the wire are placed parallelly.

Another reason to use nanowire is the consideration for the easy domain wall writing. For the impedance matching of the structures to the electrodes, the size of sample should be designed small, which causes another

problem of writing domain wall. If the coercive field of the sample is so large, then the magnetization of the sample is immediately saturated before the magnetic field is completely off. Other options for domain wall writing, such as Oersted line, is not available because the experiment has been proposed to extend to sub-ns current pulse experiment where the Oersted line is prohibited.

(a)



(b)

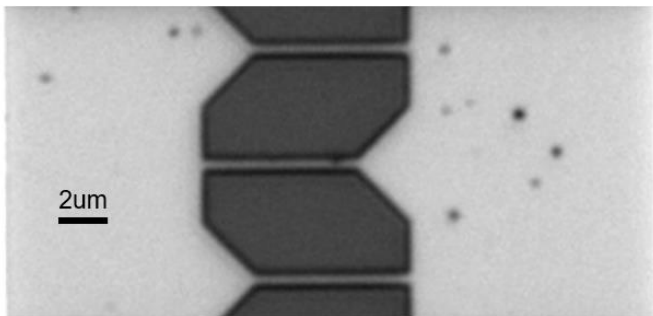


Figure 2.8 Images of the fabricated nanowire structure. (a) Scanning electron microscope image of wire of type A. (b) Optical microscope image of wire of type B.

In this situation, nanowire can be served as a barricade combining with the notch pinning effect [26]. The smaller the wire width is, the stronger the notch pinning effect on the domain wall.

The wire structures are fabricated as figure 2.8. There are two types of designs. Type A (figure 2.8 (a)) is optimized for the impedance matching, so it is proper for the high current short pulse experiment. The impedance of the wire is estimated $\sim 400 \Omega$ or more. Type B (figure 2.8 (b)) has one more parallel nano wire so the probability of finding telegraph noise site increases. Since the right-angle notch resembles the cross part of Hall bar measurement, it can be served as pre-test for electric measurement of domain wall telegraph noise. This structure is fabricated by e-beam lithography in Korea Advanced Nano Fab Center in Suwon. Electrode of the sample is then fabricated by photolithography in department 1F clean room.

2.3 Process for measuring telegraph noise

2.3.1 Procedure of measurement and data processing

Steps for measuring telegraph noise of domain wall are as follow. To write the domain wall in the sample is the first. About writing domain wall, several methods are devised to lower the nucleation field of the magnetic domain and it is presented in the next section. After writing the domain wall, drag the domain wall standing at unintended position to the one of the entrances of the nanowire where the experiment take place. Then, the detailed conditions for telegraph noise by applying field and/or current. Because the domain wall position can be displaced as the applied field and/or current change, probe beam should search around $\sim 1 \text{ um}$ with $\sim 40 \text{ nm}$ step-by-step whether telegraph noise occur. If any little telegraph noise is not founded, then reposition the domain wall in other entrance of the wire and search again. For the type (b) nanowire, there is total 6 entrances. If any hint of telegraph noise is found, then the maximize the signal by repositioning the probe position and then the position of highest signal means the center of telegraph noise site.

Figure 2.9 shows the schematic diagram of telegraph noise occurring in wire. In figure 2.9 (a), there is two conceptual lines (dashed white) of pinning sites p^+ and p^- . As explained in the introduction, telegraph noise emerges when the pinning sites are close enough to overcome the energy

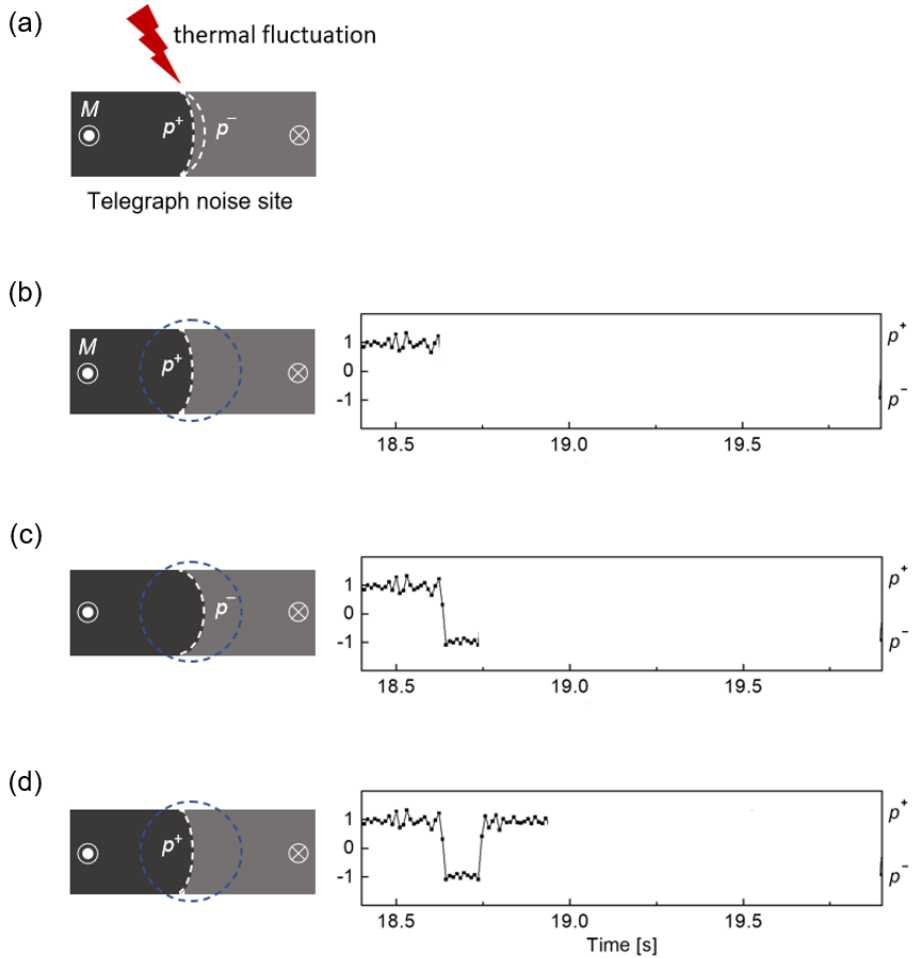


Figure 2.9 Schematics of measuring telegraph noise. Telegraph noise data on the right is normalized data for convenience of description

barrier between the pinning sites by only the thermal fluctuation, $k_B T_0$ (where T_0 is 298 K). The line of pinning sites is namely ‘conceptual’ that the domain wall thought to be pinned as the line, but real shape of domain wall cannot be determined by the resolution limit. We assume the pinning sites might be near the center of the dashed line. Figure (b) – (d) show pinning

position of domain wall and related telegraph noise development. Blue dashed circle is probe beam which is positioned on center of the site. It is explained in section 2.1.3 that telegraph noise state depends on the displacement between domain wall and probe beam. Concept picture on the left side of figures is drawn to reflect the state of telegraph noise on the right-side data.

Those plots in the figure 2.9 are not the raw data but normalized with respect to the base signal line for convenience of description. Figure 2.10 (a) shows typical raw data of telegraph noise. Drift appears in the data to the level of telegraph noise. Most of it comes from the combinational effect of wire edge and spatial drift of the sample. The raw signal jumps along the wire edge scans so, even tiny drift of the samples to the probe beam causes drift when the beam is focused near the edge. And the small signal level of telegraph noise make drift stand out much more. To overcome these defects and discriminate the state of telegraph noise, program was developed to extract the drift automatically which distinguish normal white noise and telegraph noise. Red lines in the figure 2.10 (a) is extracted drift by the program. Then the put the drift line at the center level between the up and down states of telegraph noise and normalize the data. Figure 2.10 (b) is the normalized data and (c) shows narrower view of it. What we need from the telegraph noise is the depinning time from the pinning site which contains the statistical information about the energy barrier of pinning site. It is clearly seen in figure 2.10 (c) that the

depinning times t_d^\pm of two pinning sites p^\pm are obtained unambiguously as the two states are exactly distinguished.

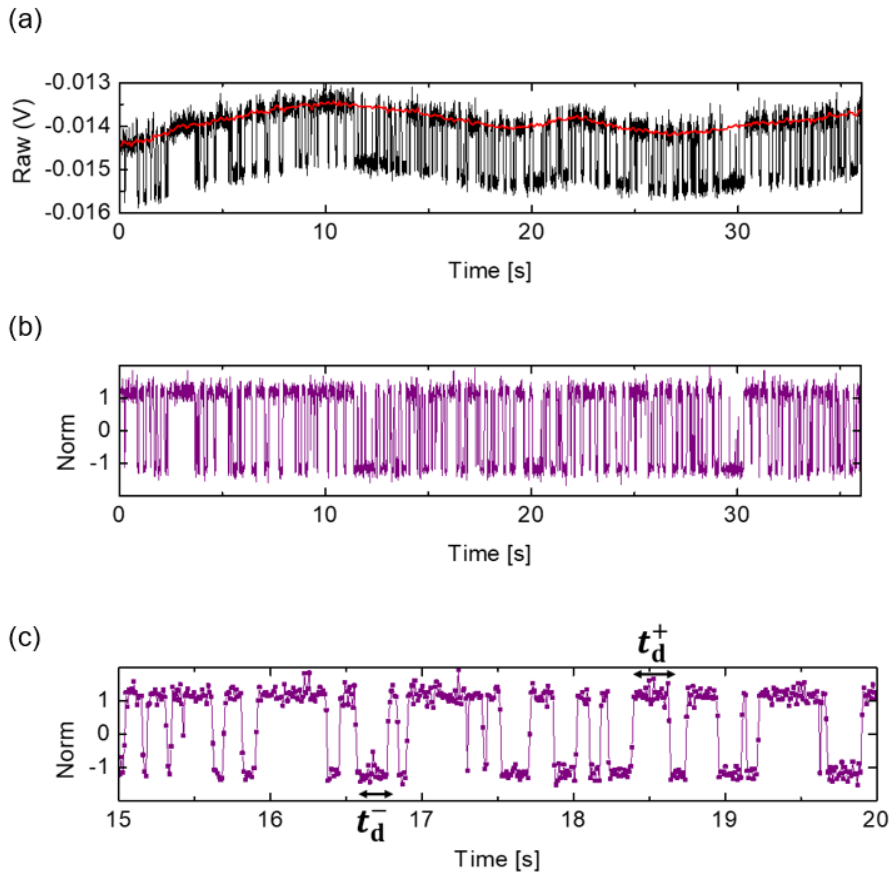


Figure 2.10 Process of telegraph noise to depinning time

Chapter 3

Depinning Energy barrier of domain wall

This chapter is dedicated to the discover of the structures of domain wall energy barrier that governs the generation of telegraph noise. By analyzing the depinning times, it turns out that stochasticity of the telegraph noise follows certain statistic features. Energy barrier of the domain wall depinning is related to the average depinning time by Arrhenius law of activation. Telegraph noise appears different features in different conditions of magnetic field or electric current. Energy barrier extracted in a large amount of the various conditions are investigated, revealing relationship of domain wall depinning energy barrier to field and current. Analytic formula of the energy barrier is derived to discover the physical meaning of the relationship. Complete picture of the energy landscape of telegraph noise comes from incorporating analytic formula into the experimental results.

Section 3.1 introduces the motivation and background of this chapter. Experimental information is also provided in this section. In **Section 3.2**, statistics of the telegraph noise is examined, and the energy barrier is induced from the statistics. In **Section 3.3**, experimental result of energy barrier in several field and current conditions are presented and discussed. Analytic

formula of the domain wall depinning energy barrier is derived in **Section 3.4**.

This chapter conclude in **Section 3.5** with summary.

3.1 Introduction

3.1.1 Motivation and background

Depinning energy barrier of domain wall has been one of the interested topics in understanding domain wall dynamics [15,17,18,20]. In academical aspects, determining which mechanism is mainly working for depinning domain wall is one of the interests. Another interest is about the harmonic motion at pinning site in which effective mass of domain wall can be measured by resonating motion of the domain wall with harmonic potential assumption [27]. In application aspects, electric current dependence of domain wall energy barrier has been a major issue as it governs the two important properties for device that are paradoxical to each other: the stabilities and the energy consumption. In the racetrack model [15], which is a representative model of the application, the more stably a domain wall is pinned at strong pinning sites when off state, the more energy it consumes to depin the domain walls when powered on.

Although the depinning energy barrier is considered important and a lot of experiment has been done by several method [16,17], there is some unwilling points innated in the experiment. One example is that it needs a lot of samples to make clear statistics of the depinning time. Many experiments gather statistics as many as possible for reliability of the data, but it is much important in domain wall depinning experiment because the depinning

phenomenon are governed by stochastic behavior of thermal activation. So, it exactly needs the distribution of counts of depinning time, not just the mean or standard deviation of the data. The statistics becomes clearer as the more data is gathered, but it also takes much time. Other example of unwilling point is that to repeat the experiment for gathering more depinning time, repeated tasks of writing and positioning the domain wall at pinning site is needed. Writing and positioning the domain wall accompanies the field and/or current application which causes adverse effect to the setup and thus signal.

Opposite to those issues, in telegraph noise measurement, pinning and depinning of domain wall occurs repeatedly and spontaneously without any dynamic input of field or current. And depending on the telegraph noise sites, the samples of depinning time can be gathered to the rate of $\sim 100/\text{min}$ in constant condition. Moreover, telegraph noise is in definition generated by two (or more) pinning sites, which means that it provides depinning time of two (or more) pinning sites at the same time. Experiments for two (or more) pinning sites can be executed simultaneously.

Here, the difference of this study to the previous work [19] is explained. At first, the system is different, which means it is different not just for the chemical composition, but for the governing mechanism of domain wall dynamics. Differences in Pt/Co/W (this study) to Pt/Co/Pt (the previous) is that Pt/Co/W shows high Dzyaloshinskii-Moriya interaction [28–32] and spin-orbit torque [32–34] is dominant mechanism of current-induced domain wall motion.

Experimental conditions also different, especially for the current waveform. Here, we apply dc electric current to see the basic relation of the domain wall depinning with the current, which is different from the pulsed current generated by photoconductive switch used in previous work. Effect of dc current and pulsed current can differ because the pulsed current can occur dynamic effect. Finally, only one pinning site are studied in the previous study. In this study, all the information from pinning sites is exploited to understand phenomena related to telegraph noise.

3.1.1 Experimental information

The sample used in this study is Ta (1.5 nm)/Pt (3.0 nm)/Co (1.0 nm)/W (5.0 nm)/TaO_x(2.0 nm) heterostructures deposited on the Si/SiO_x substrate. The film is fabricated to the nanowire of type B structure, and the telegraph noise site is selected at the left entrance of 2nd wire (figure 3.1). Other detailed information of the sample preparation is the same as explained in the section 2.2.

To apply current on the sample, wire bonder (Kulicke & Soffa) is used to connect the electrode of the sample to the printed circuit board (PCB). The PCB is custom designed to fit the sample holder. Detailed design of the PCB is on the appendix. Electromagnet (customized, KR Tech) is used to apply magnetic field which is controlled by analogue output source (PCI-6711, National Instrument). Function generator (AFG3052, Tektronix) is used as a

current source.

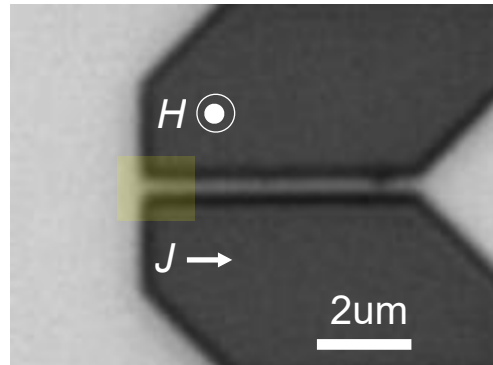


Figure 3.1 Microscope image of experimental spot. Yellow mask indicates the spots and nearby. Direction of field and current indicates the plus sign

3.2 Energy barriers E_B of telegraph noise

3.2.1 Statistics of depinning time t_d

Raw data of telegraph noise itself provides little information about the system. Depinning time of the domain wall should be collected from the data to make meaningful statistics. Here, the depinning time in the data indicates the dwelling time in certain state of telegraph noise. As the notation of the figure 2.10, two pinning sites are named p^\pm , whose level correspond to the ± 1 of normalized telegraph noise. Depinning time of the pinning sites t_d^\pm is simply the time length of the signal dwelling in ± 1 before transition. Obviously, the transition from ± 1 corresponds to the domain wall depinning from the pinning site p^\pm . In this section, the statistics of depinning time t_d^\pm is presented as an example. Applied magnetic field are the same as -1.12 mT for the data in section 3.2.

Statistical analysis of telegraph noise presented below is for the case of t_d^- as an example. Figure 3.2 (b) shows the count of t_d^- measured in $H = -1.12$ mT and $J = 2.24 \times 10^{10}$ Am². Count of depinning time t_d^- decays from the lowest bin of the histogram. The red patterned bar shows the cumulative count of the histogram. Although it seems that the histogram decays exponentially at first glance, it is not so clear. To better understand the statistics, counts are normalized to represent as distribution function. Figure 3.3 (a) is the cumulative distribution function $F(t_d^-)$ (solid black) and $1 - F(t_d^-)$ (dashed

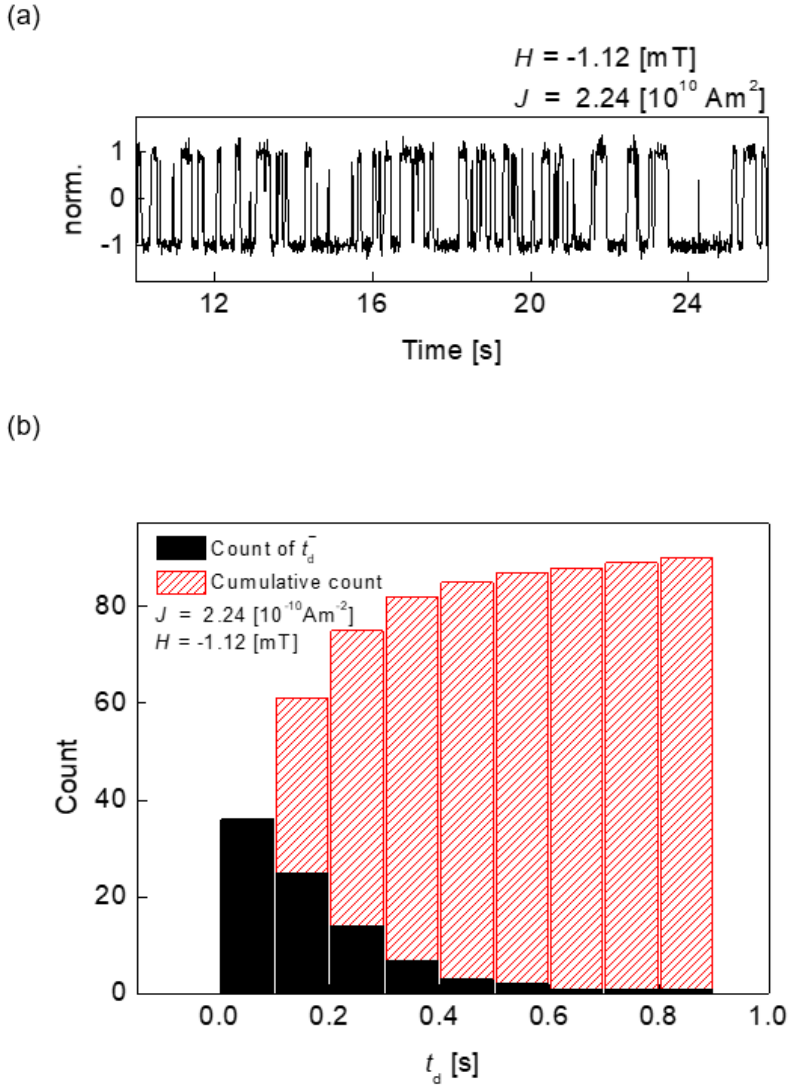


Figure 3.2 Example measurement for the statistic research. (a) normalized telegraph noise. ~ 90 samples are obtained for t_d^\pm each in one measurement for 30 s. (b) Histogram and cumulative count of the t_d^- .

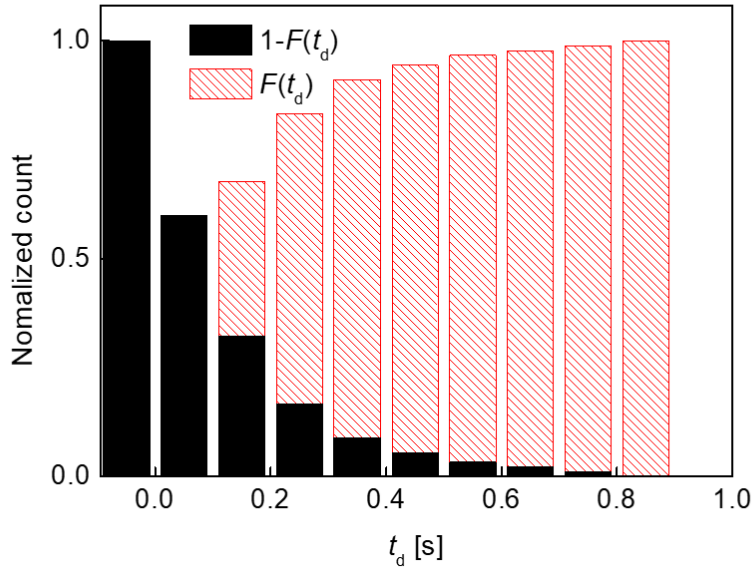
red), both of two contain the trivial value of 0 (or 1 in $1 - F(t_d^-)$ case) on the bin of negative depinning time. When the representative value of the bin is end value, then the meaning of the $F(t_d^-)$ becomes the probability of the system

showing depinning time below t_d^- . Likewise, $1 - F(t_d^-)$ is the probability of the system showing depinning time above t_d^- . In this figure, exponential decay is clearly shown on the $1 - F(t_d^-)$ plot.

To understand this statistical feature, Poisson statistics is adopted in this phenomenon [35]. Poisson distribution tells us the probability of the k number of events occurring in time t , given the rate of event occurrence is fixed to r . The distribution equation is given by $P(k; t) = (rt)^k \exp(-rt)/k!$, where the variables are as mentioned previously. This equation also tells us the probability of waiting time T until the next event. With the definition of the formula, put T in t and 0 in k , then the probability $P_T = \exp(-rT)$ comes out. This is the concept of arrival time T in Poisson distribution.

The concept of arrival time is analogous to the depinning time in this study. The event corresponds to depinning, arrival time does to depinning time and the P_T does to $1 - F(t_d^-)$ which show clear exponential decay like formula. As the results fits well in the Poisson distribution, it can be said that depinning phenomena in this telegraph noise site are governed by single path, the rate of which is the coefficient of the exponent. Instead of using rate, we call the exponent coefficient of fitting parameter to be time constant τ^\pm by assuming $1 - F(t_d^-) = \exp(-t_d^\pm/\tau^\pm)$. Figure 3.3 (b) shows the $1 - F(t_d^\pm)$ and fitting of that those in log scale. From the fitting, τ^+ and τ^- result in 159 and 91 ms each. It is noticeable that the τ gives the expectation value of t_d if the number of samples is large enough to fit well to the exponential curve.

(a)



(b)

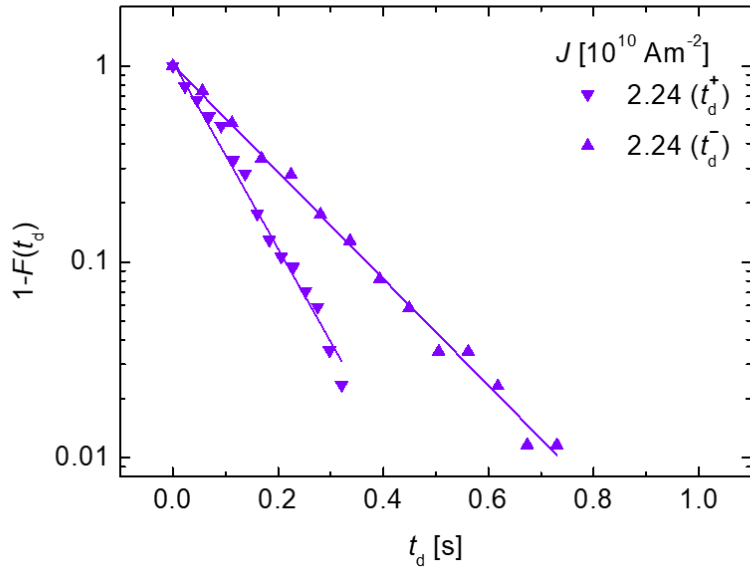


Figure 3.3 (a) $F(t_d^-)$ (solid black) and $1 - F(t_d^-)$ (dashed red) of the depinning time t_d^- . (b) Log plots of $1 - F(t_d^\pm)$ and the fitting line

Figure 3.2 (a) clearly shows the differences of two time constant as the most of t_d^+ is short and the most of t_d^- is long.

3.2.2 E_B^\pm from the statistics of depinning time t_d

It is well known that, when the thermal activation is dominant, the rate of the overcoming the energy barrier is governed by Arrhenius law. As domain wall depinning phenomena is well known example of thermally activated process [36–38], we adopt the Arrhenius law to extract energy barrier E_B^\pm of domain wall depinning from p^\pm . The rate r introduced in the Poisson distribution is related to the rate of activation in Arrhenius law as follows. $r^\pm = 1/\tau^\pm = f_0 \exp(-E_B^\pm/k_B T_0)$, where f_0 is attempt frequency which is assumed 1 GHz [37], k_B is the Boltzmann constant, and T_0 is the temperature of the laboratory which is about 298 K. Converting the formula of rate into the form of energy barrier of domain wall depinning is given by

$$E_B^\pm = k_B T_0 \ln \frac{\tau^\pm}{\tau_0} \quad (2)$$

where the $\tau_0 = 1/f_0$. With this relationship, energy barriers are obtained as 18.3 and 18.9 $k_B T_0$ for p^+ and p^- each. Differences in energy barriers can be witnessed indirectly with the raw data in figure 3.2 (a) where the depinning rate of p^+ is faster than that of p^- .

Finally, it should be noticed that generation of telegraph noise investigated in this study is governed by the single energy barrier scheme. It

can be verified by the exponential relation of $1 - F(t_d^{\pm})$, combining with discussion on properties of system governed by Poisson distribution in section 3.2.1. There have been some domain wall depinning experiments [16,18] reporting the modified exponential distribution which can be seen in a system with multiple depinning paths.

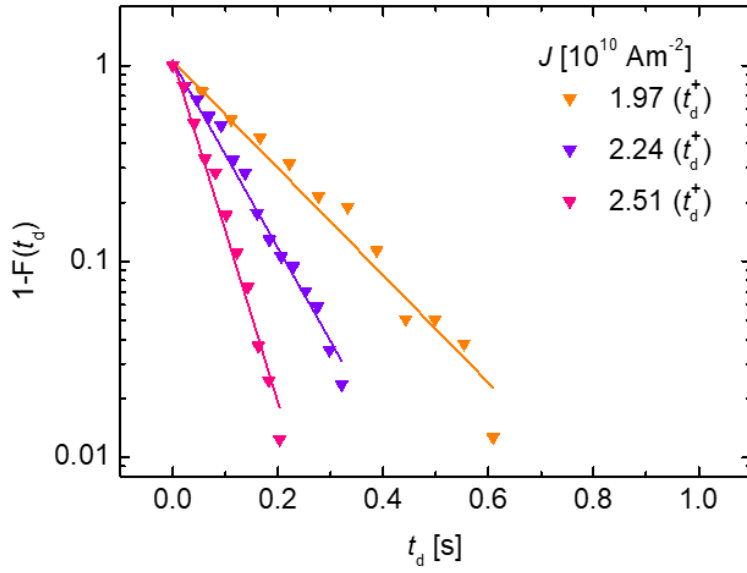
3.3 Dependence of energy barrier E_B on magnetic field H and electric current J

In the previous section, domain wall depinning energy barrier is extracted in $H = -1.12$ mT and $J = 2.24 \times 10^{10}$ Am². In this section, energy barrier is obtained in various magnetic field H and electric current J to set energy barrier function $E_B^\pm(H, J)$. As a starting point, $1 - F(t_d^\pm)$ under several current is examined. Then E_B^\pm in different conditions are obtained using the equation (2) and $E_B^\pm(J)$ will be obtained for each field conditions. Finally, whole relationship to the field and current will be established using fitting results of each $E_B^\pm(J)$ s.

3.3.1 Statistics in different current density

Figure 3.4 (a) show the $1 - F(t_d^+)$ of t_d^+ in three different current conditions of certain step under constant field of $H = -1.12$ mT. It can be seen in figure 3.4 that slope of the $1 - F(t_d^+)$ gets steeper as the current increases, meaning that the time constant τ^+ gets faster. From the low current to high current, τ^+ decreases to 158.7, 91.2 and 49.8 ms. Thus, corresponding E_B^+ decreases to 18.9, 18.3 and 17.7 $k_B T_0$. It seems that as the current increases at regular steps (0.27×10^{10} Am⁻²), E_B^+ also decreases at certain steps ($0.6 k_B T_0$). To see certain linear relationship, applied current range

(a)



(b)

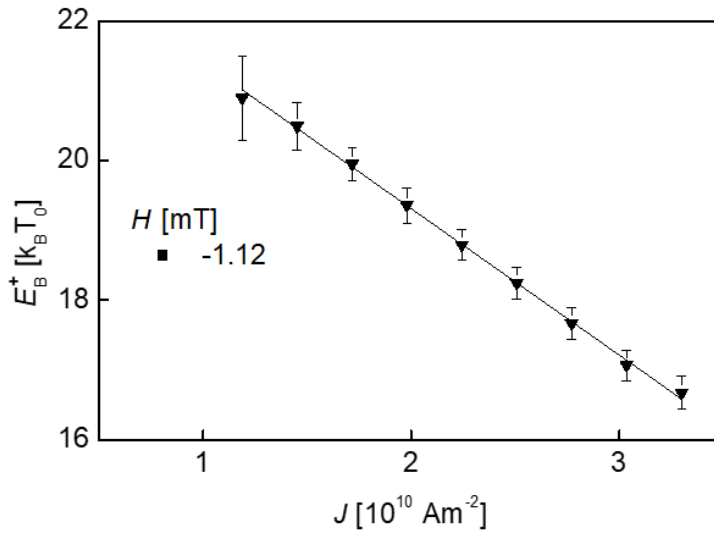


Figure 3.4 (a) $1 - F(t_d^+)$ of three different applied current in certain step and in constant field. (b) E_B^+ in various applied current. Three points in center correspond to the results (a).

increases with the same step. Figure (b) show clear linear relationship of E_B^+ to the applied current. Each point is average of E_B^+ s obtained from ~ 40 repeated measurement, each of which takes 30 s. The measurement was repeated cyclically in current to avoid any environmental fluctuation such as temperature which causes a crucial difference on energy barrier estimation. To mention briefly, temperature of the laboratory is regulated by thermo-hygrostat by 25°C and it is known after the temperature experiment in chapter 4 that the temperature of the sensor in contact with the sample fluctuate under $\pm 0.1^\circ\text{C}$.

To complete the dependence of both $E_B^\pm(H, J)$, experiment is designed to sequence the measurement in 2-D field and current mesh. The sequence of the measurement is as follow. First, measure telegraph noise in a row of increasing current step and constant in field. After 1 current cycle is finished, increase the field by certain step and do current cycle again. Applied field ranges from -1.12 to 1.12 mT. After finish 1 cycle of field, then it means 1 whole field and current cycle finished so, repeat the cycle from -1.12 mT.

Figure 3.5 is the E_B^\pm of various field and current obtained by ~ 40 repeated measurement for each point. Upper plot of figure is plot of E_B^+ and lower one is that of E_B^- . Error bars correspond to the standard deviation of the E_B^\pm s from ~ 40 times measurement. As in the figure, applied current in each constant field shows linear dependency. Moreover, the line of each constant field shows constant interval, which suggest that the E_B^\pm has linear dependence on applied field H too. As the field increases (or the color of the plot get

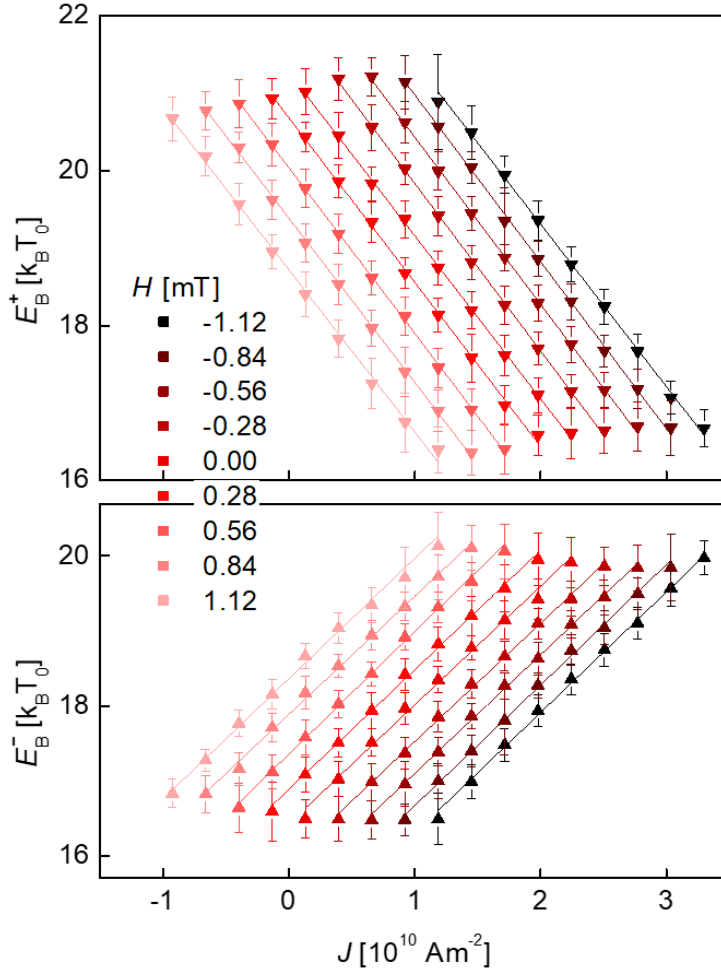


Figure 3.5 E_B^\pm in various applied field and current. Upper plot is E_B^+ and lower one is E_B^- .

blurrier), in the same applied field E_B^+ decreases and E_B^- increases. So, it means that field and current work same directions for each pinning site and the composite force of field and current exert in opposite with respect to each

pinning site.

With this result, H and J dependence of E_B^\pm is investigated by assuming the linear relation of the E_B^\pm as

$$E_B^\pm(H, J) = E_0^\pm + a^\pm(H + \varepsilon^\pm J) \quad (3)$$

To get those parameters in the equation (3), fitting of the figure 3.5 is used so the slope of the fitting correspond to the $a^\pm \varepsilon^\pm$, and the y-intercept of the fitting

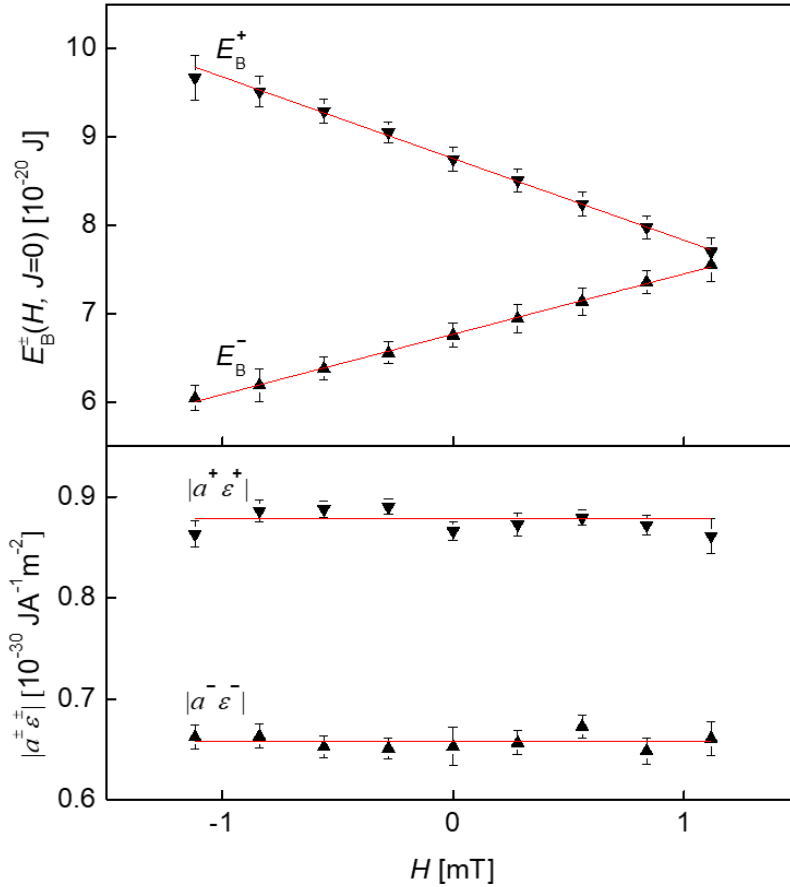


Figure 3.6 Plot of y-intercept (upper) and slope (lower) of fitting results of figure 16.

correspond to the $E_0^\pm + a^\pm H$. Figure 3.6 is the plot of y-intercept and slope of fittings. Error bars of upper plot are maximum error of each applied field and those of lower one is standard error of the fitting. It is clearly seen in the upper plot that field dependence of the E_B^\pm also shows linear dependency. And the lower plot shows the constant value with different sign ($a^\pm \lesseqgtr 0$). These result shows that the linear assumption works well in this system. With further fitting on those plots, whole parameters of linear relation are extracted in Table I. for each pinning site p^\pm .

Table I. Extracted values of E_0 , a , ε

Site	E_0 ($k_B T_0$)	a (10^{-18} J/T)	ε (10^{-14} Tm ² /A)
p^+	21.4 ± 0.7	-9.2 ± 0.2	9.5 ± 0.5
p^-	16.3 ± 0.5	6.8 ± 0.1	9.6 ± 0.5

3.3.2 Analytic formulation of energy barrier

Although the E_B^\pm can be expressed as a linear function of H and J , physical meaning of parameters on Table I. is uncertain. To physically interpret that linear relationship, energy barrier of the domain wall depinning is derived analytically. Overall procedure for the derivation follows the theoretical work for domain wall energy barrier of spin-transfer torque system [20]. Mechanism

for configuring and driving the domain wall differs from the above theoretical works. Take driving mechanism for example first, spin-orbit torque is the dominant mechanism for current-induced domain wall motion [39], which is completely different from the spin-transfer torque in mathematical formulation. For the domain wall configuration, the type of domain wall in this study shows Néel-type wall in which magnetization toward the wall normal is supported by strong Dzyaloshinskii-Moriya interaction (DMI) [39]. Except for the mechanism, procedure for derivation is as follows. Domain wall motion is assumed to be 1-D collective model in which the motion is represented by domain wall position q and domain wall magnetization ψ . To describe the motion of unit magnetization of the system, the Landau-Lifshitz-Gilbert (LLG) equation [40] of the system can be written as follow.

$$\frac{d}{dt}\vec{m} = -\gamma_0\vec{m} \times \vec{H}_{eff} + \alpha\vec{m} \times \frac{d}{dt}\vec{m} + \gamma_0\tau_{DL}\vec{m} \times (\vec{m} \times \hat{y}) \quad (4)$$

where, \vec{m} is unit magnetization, γ_0 is gyromagnetic ratio, α is damping constant, y is the direction of wire width, τ_{DL} is damping-like portion of spin-orbit torque [41]. H_{eff} is effective field which is summation of $H_{eff} = H_{ex} + H_{exchange} + H_{aniso} + H_{demag} + H_{DMI} + H_{pin}$ where, H_{ex} is external field, and $H_{exchange}$, H_{aniso} , H_{DMI} , H_{demag} are effective field by exchange interaction, anisotropy field, DMI and demagnetization field. H_{pin} is the pinning force when the domain wall is pinned at harmonic potential. Assumed equation of magnetization on the wire is as follow.

$$\begin{cases} m_x = \cos \psi \operatorname{sech} [(x - q)/\lambda] \\ m_x = \sin \psi \operatorname{sech} [(x - q)/\lambda] \\ m_z = -\tanh [(x - q)/\lambda] \end{cases} \quad (5)$$

where λ is width of domain wall. By substituting equation (5) in (4) and integrating over the whole wire, equation of motion of domain wall is as follow.

$$\begin{cases} \alpha \frac{\dot{q}}{\lambda} + \dot{\psi} = \gamma_0 (H_z^{ex} - \varepsilon_{SOT} J \cos \psi) - \frac{\gamma_0}{2M_S \Omega} \frac{\partial}{\partial q} V(q, \psi) \\ \frac{\dot{q}}{\lambda} - \alpha \dot{\psi} = \frac{\gamma_0}{2M_S \Omega} \frac{\partial}{\partial \psi} V(q, \psi) \end{cases} \quad (6)$$

where M_S is saturation magnetization, Ω is cross section of the wire, and $V(q, \psi)$ is pinning potential by which the H_{pin} is generated. τ_{DL} is converted into the function of current and angle of magnetization $\varepsilon_{SOT} J \cos \psi$ with coefficient ε_{SOT} .

After deriving the equation of motion, effective Lagrangian is derived equation of which is the same as equation (6). The Lagrangian L and dissipation function F satisfying the equation (6) is as follows.

$$\begin{cases} L = \frac{M_S \Omega}{\gamma_0} (\dot{q} \psi - q \dot{\psi}) - V(q, \psi) + 2M_S \Omega q (H_z^{ex} - \varepsilon_{SOT} J \cos \psi) \\ F = \alpha \frac{M_S \Omega}{\gamma_0 \lambda} \left(\dot{q}^2 + \lambda^2 \dot{\psi}^2 + 2q \dot{\psi} \frac{\gamma_0 \lambda}{\alpha} \varepsilon_{SOT} J \sin \psi \right) \end{cases} \quad (7)$$

Then, the effective energy of the domain wall near the pinning site can be derived by Hamiltonian as follows,

$$E(q, \psi) = V(q, \psi) - 2M_S \Omega q (H_z^{ex} - \varepsilon_{SOT} J \cos \psi) \quad (8)$$

And the pinning potential $E_0(q, \psi)$ is assumed to be harmonic near the potential extrema, which is given by

$$V \simeq \begin{cases} \omega_G^2(q - q_{G0})^2 + v_G^2(\psi - \psi_{G0})^2 & \text{near } (q_{G0}, \psi_{G0}) \\ E_0 - \omega_S^2(q - q_{S0})^2 + v_S^2(\psi - \psi_{S0})^2 & \text{near } (q_{S0}, \psi_{S0}) \end{cases} \quad (9)$$

where q_{G0} is position of energy minima of pinning point, q_{S0} is energy maxima of saddle point of energy barrier and E_0 is the potential difference between pinning site and saddle point, all of which are without any application of field and current. When the field or current is applied, new energy extrema q_G, q_S, ψ_G, ψ_S can be derived by applying equation (9) into (8). Then, energy barrier of given system is given by energy difference between saddle point and pinning ground, in other words, $E_B = E(q_S, \psi_S) - E(q_G, \psi_G)$. In the derivation, it is assumed that the ψ dependency is negligible. Then the analytic form of energy barrier between the pinning site and the saddle point is given by

$$E_B = E_0 - 2M_S\Omega\delta(H - \varepsilon_{SOT}\cos\psi_{G0}J) \quad (10)$$

where $H = H_z^{ex}$ and $\delta = q_{S0} - q_{G0}$ meaning the displacement of saddle point from the pinning site. Although we assuming that the angle ψ is unchanged for the derivation, combining the result of the ε^\pm in the Table I, which corresponds to $\varepsilon_{SOT}J\cos\psi$ in this analysis, assumption works well because of both ε^\pm are the same value within the error. Otherwise, if the ψ changes during the depinning from pinning site p^+ to p^- , the ε^\pm would be different because of the coefficient $\cos\psi_{G0}$. Therefore, combining the angle dependent value of $\varepsilon_{SOT}J\cos\psi$ to be effective value, we can finalize the energy barrier formula to be as follows.

$$E_B = E_0 - 2M_S\Omega\delta(H + \varepsilon J) \quad (11)$$

With this result, we can extract the other parameter δ which is related to the physical length from pinning site to the saddle point.

Table II Displacement to the saddle point from each pinning sites

Site	δ (nm)
p^+	8.9 ± 0.2
p^-	-6.6 ± 0.1

As we set the sign of q to be from p^\pm to p_s , these result matches well in the sign as the energy saddle point is between two pinning sites. Figure 3.7 describes energy landscape of the experiment site according to the extracted parameters.

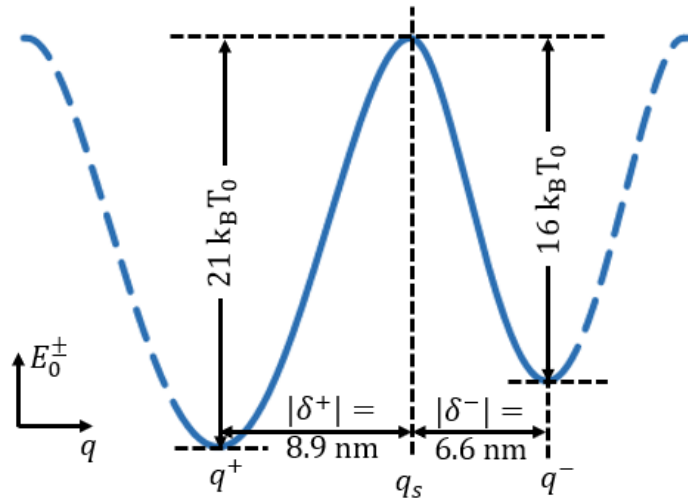


Figure 3.7 Energy landscape of telegraph noise site

3.3.3 Discussion on the parameters

Distance between two pinning sites of telegraph noise is estimated to be 15.5 ± 0.4 nm by summing the result of δ^\pm . This distance can also be estimated from optical signal based on ratio of signal level of telegraph noise to the full switching signal of MOKE. Adopting computational method explained in section 2.1.3, it is estimated optically to be ~ 20 nm which is consistent with energy barrier analysis within the order of few nanometers. However, assumptions for the estimate need to be reviewed. Most critical assumption concerns the domain wall arrangement on the wire. It is assumed that each end of domain wall is pinned at both edges of wire and pinning sites p^\pm lie on the center of the wire, so the domain wall bulges up and down as telegraph noise occur, as illustrated in figure 10. The optical estimates can be several orders of magnitude larger depending on what the shape of area swept by domain wall looks like.

Effective field coefficient ε^\pm is compared with the other report of the same system [39]. In this reference, the ε is estimated to be $14 \times 10^{-14} \text{ Tm}^2\text{A}^{-1}$ which is slightly bigger than this experiment but agrees well within the order. Interesting point is that ε of both pinning sites are almost the same with each other, supporting the claim that the magnetization of domain wall is preserved for each site. This can be inferred from the difference of the origin which controls the domain wall motion. Pinning site of the domain wall

is largely affected by the defect of magnetic layer, but current-induced domain wall motion is affected by the spin-hall effect from the nonmagnetic layer. If the defect of pinning sites does not affect nonmagnetic layer, then this result is sufficiently possible to occur.

Natural pinning potential E_0^\pm and length-dependent coefficient a^\pm are also compared to the other studies of the Pt/Co/MgO [17] and Pt/Co/Pt [19] system. Study on the Pt/Co/MgO reports E_0 and $|a|$ as $34 k_B T_0$ and $15 \times 10^{-18} \text{ JT}^{-1}$ and study on Pt/Co/Pt reports those as $20 k_B T_0$ and $21 \times 10^{-18} \text{ JT}^{-1}$, parameters of which are similar to this study. Summarizing all the results together, magnitude of a seems to follow that of E_0 . This correlation can be thought of as evidence for the origin of pinning site associated with the physical obstacle with finite length. Further investigation can solve the question of the correlation by collecting statistics of those parameters from multiple pinning sites, and the method using telegraph noise provides advantageous for future work as many pinning sites can be investigated simultaneously and quickly.

3.4 Summary of chapter 3

Structure of energy barrier of telegraph noise is thoroughly investigated by analyzing statistics of telegraph noise. $1 - F(t_d^{\pm})$ exhibit a clear exponential decay showing that telegraph noise of the system is generated by single energy barrier. With the assumption of Arrhenius law of activation, energy barrier is obtained from the time constant τ of telegraph noise. Energy barrier E_B is investigated in different applied field and current, which result in clear linear dependence of the E_B on H and J . To extend the understand of the relationship, analytic formula of E_B is derived where the domain wall represents Nee-type configuration by Dzyaloshinskii-Moriya interaction and its motion is dominated by spin-orbit torque. Distance between two pinning sites is estimated to be ~ 15 nm by linear coefficient of E_B , which is comparable to the estimation by optical signal. Natural pinning potential and spin-torque efficiency are also within order of other studies on energy barrier. The findings of the study could be a starting point for device application of the telegraph noise by domain wall motion.

Chapter 4

Verification of Arrhenius Law

In the previous chapter, information of energy barrier is obtained by assuming Arrhenius law of activation. In this chapter, we verify whether the assumption is correct by measuring telegraph noise with different temperature conditions. For that, in **Section 4.1**, add-on setup for the exist MOKE microscope is designed optimized for the temperature experiment. Result is shown with the brief discussion in **Section 4.2**.

4.1 Add-on setup for temperature experiment

Setup for temperature experiment is built by reforming sample stage in which thermal components are added while leaving the other parts as they are. As can be seen in figure 4.1 (a), space for the sample stage is limited by huge magnet cores. To overcome this limitation and secure enough space for the additional components, rectangular stage with high aspect ratio is designed so that it has free space through the horizontal axis and section for attachment at head and tail. Figure 4.1 (b) and (c) shows the complete assembly of temperature-adjustable stage.

Revision of sample stage

Temperature of sample is controlled by two 20 W ceramic heaters. Advantage of this ceramic heater is that it can passively regulate temperature only with constant voltage application by its positive temperature coefficient. The heaters covered with aluminum shield are placed on two far ends of the back of the stage, which are fixed by the copper tape. Symmetric arrangement of heaters is for minimizing temperature gradient which might cause any temperature induced magnetization effect [42]. Voltage of heater is controlled by power supply (E3649A, Agilent) connected red and blue cable in the figure. Stage is made of copper which is expected to conduct heat well from the back side of the stage to the whole part. In the front side of stage,

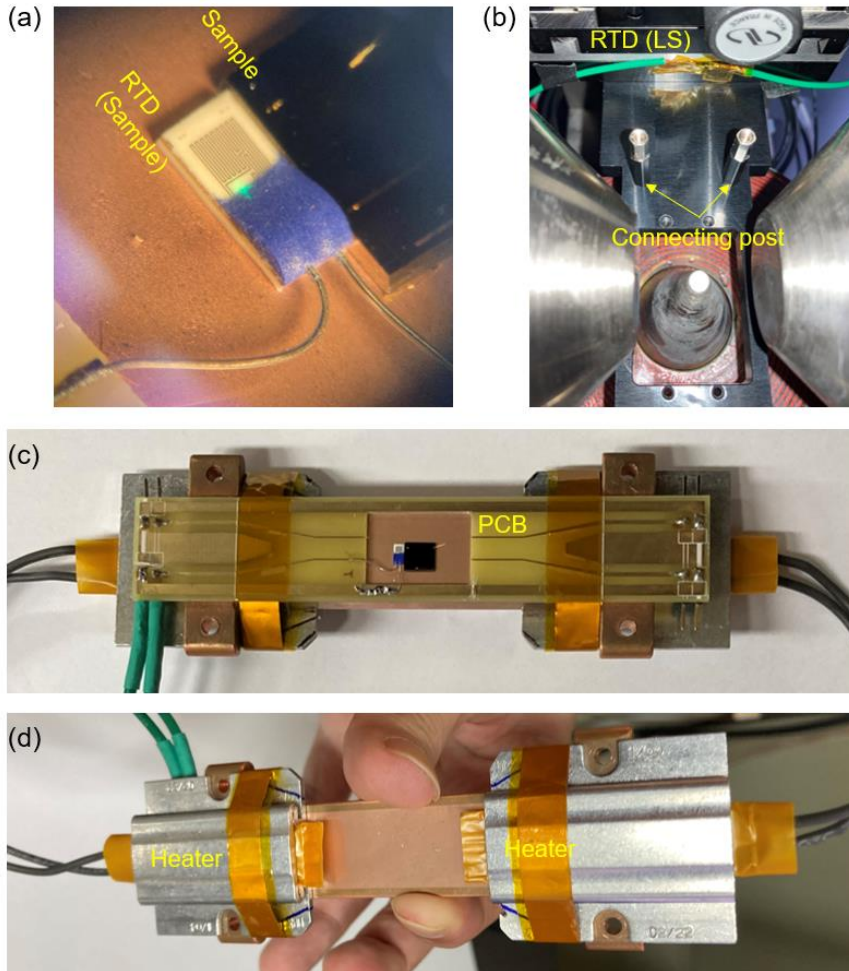


Figure 4.1 Outlook of add-on setup for temperature experiment. (a) Zoom-in image of sample substrate and RTD. (b) Image of space for sample stage and connecting post. (c) and (d) Front and back side image of sample stage with heater

printed circuit board (PCB) of coplanar wave guide structure is installed. Sample space is drilled square in the center of the PCB, so the sample substrate directly contacts to the stage. Kapton tape winds up heaters and PCB together on the stage to hold components.

Temperature of the sample is measured by thin film resistive temperature detector (RTD) made of Pt. Temperature coefficient of resistance between 0 °C and 100 °C is 3850 ppm/°C and the resistance at 0 °C is 100Ω, which is standardized values for RTD named after ‘PT100’. With this quantities, temperatures of the system contacting to the sensor can be measured under 0.1 °C resolution. Two RTD is used for the experiment. One is to measure temperature near sample which can be seen in figure 4.1 (b). It is placed right below the sample substrate whose connection extensions are soldered on isolated part of PCB which is prepared for temperature measurement only. Resistance of the RTD near the sample is measured by the digital multimeter (DMM 2000, Keithley) two-point probe with green cables. Another RTD is attached on the XY linear stage (figure 4.1 (a)). Because the setup is built by adding up thermal components on the existing equipment, which is optimized for room temperature, effect of temperature increment on the equipment should be checked. For the case of XY linear stage, it is precision machinery whose guaranteed operation temperature is from 20 °C to 35 °C, storage temperature of which is only 40 °C. It is thermally contacted with the heater so for the safety of the linear stage it should be checked whether the temperature of linear stage goes over the threshold while the sample stage heats up. Resistance of this RTD is measured with DAQ by applying small alternate current on the RTD. To isolate the heat from the sample stage, posts connecting sample and linear stage are replaced by those made of nylon which has low

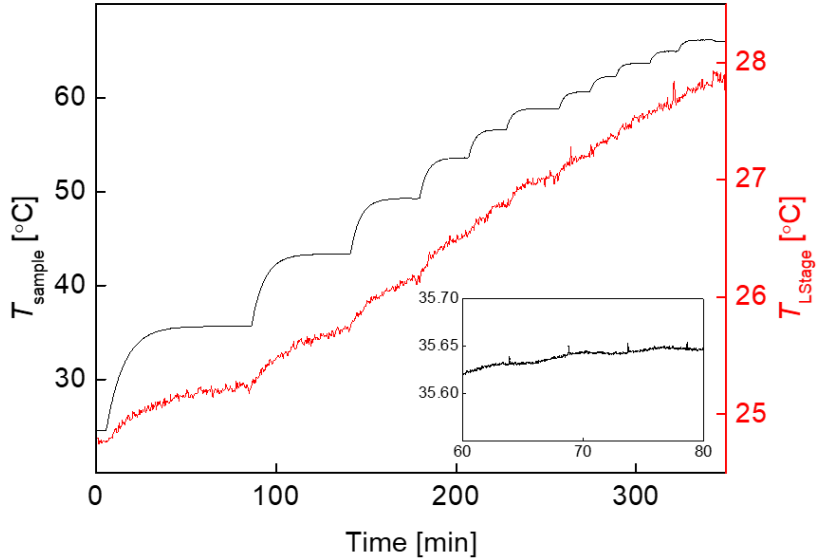


Figure 4.2 Test result of temperature measurement. Black line is temperature of sample stage and red line is temperature of linear stage. Inset plots first plateau of sample stage temperature ($\sim 35\text{ }^{\circ}\text{C}$)

thermal conductivity (figure 4.1 (a)).

Test result of temperature control

Test results for the temperature setup is in the figure 4.2. The figure shows the measured temperature in time where the heaters run from 0 V to maximum applicable voltage of 24 V. Temperature of the sample (black) recorded from the $25\text{ }^{\circ}\text{C}$ (room temperature) to $65\text{ }^{\circ}\text{C}$, showing clear steps for each applied voltage, while the temperature of linear stage is far under $35\text{ }^{\circ}\text{C}$. Stability of the temperature of sample stage can be seen in the inset of figure

4.2 which is magnified image of the first plateau of 4 V applied field. Temperatures stabilizes within 0.05 °C ranges over the 20 min in which nearly over 4000 samples of depinning time can be obtained. Little spikes of ~0.02 °C is due to the renewal sequence of resistance measurement of multimeter which does not affect the telegraph noise measurement.

Significance of the result is that detailed setup and method for temperature experiments is established which is uninterrupted to the exist MOKE microscope. Electromagnet is one of the essential components of MOKE microscope, which is confines the space of the sample. By adopting the sample stage developed in this section, stabilized temperature measurement will be available without much correction on the exist setup. Operational range can be enlarged by several methods for example, using heater of higher power ranges, reducing the mass of the copper stage, or replacing connection post from the polymer to ceramic ones to improve the heat isolation inside the stage.

4.2 Result and discussion

Experimental spot and detailed method to collect statistics of depinning time is the same as those of previous chapter. Measurement was done under the current $J = 0.56 \times 10^{10} \text{ Am}^{-2}$ with zero magnetic field. Power of probe beam is $42.5 \text{ } \mu\text{W}$. Figure 4.3 (a) shows the telegraph noise measured at $24.9 \text{ } ^\circ\text{C}$ (upper) and $35.2 \text{ } ^\circ\text{C}$ (lower). Clear difference of rate of oscillation in temperature can be seen in the figure that data of $35.2 \text{ } ^\circ\text{C}$ oscillates faster than that of $24.9 \text{ } ^\circ\text{C}$, as expected by Arrhenius law.

Depinning time constant τ_d^\pm between this range is plotted on the figure 4.3 (b). τ^+ (Inverted triangle) at each temperature lie above τ^- (Normal triangle) which can be inferred by the figure 4.3 (a). Both τ_d^\pm decrease as temperatures increase. Plots are fitted by the equation $\tau_d^\pm = \tau_0 \exp(E_B^\pm/k_B T)$ where τ_0 is fixed to 1 ns as done in the chapter 3. It can be seen that the lines assumed by the Arrhenius law fits well within error bar of the result which is obtained by standard deviation of data set. Energy barriers E_B^\pm derived by the fitting is $E_B^+ = 7.52 \pm 0.09 \times 10^{-20} \text{ J}$ ($= 18.3 \text{ } k_B T_0$) and $E_B^- = 7.29 \pm 0.13 \times 10^{-20} \text{ J}$ ($= 17.1 \text{ } k_B T_0$) where $T_0 = 298 \text{ K}$. Obtained energy barriers are well within the range of the figure 3.5 in chapter 3.

Deviation from the trend line is speculated for several possibilities. One thing is deficiency of sample compared to the previous chapter. Total measuring time of each point in plot is about half or less than that of each point

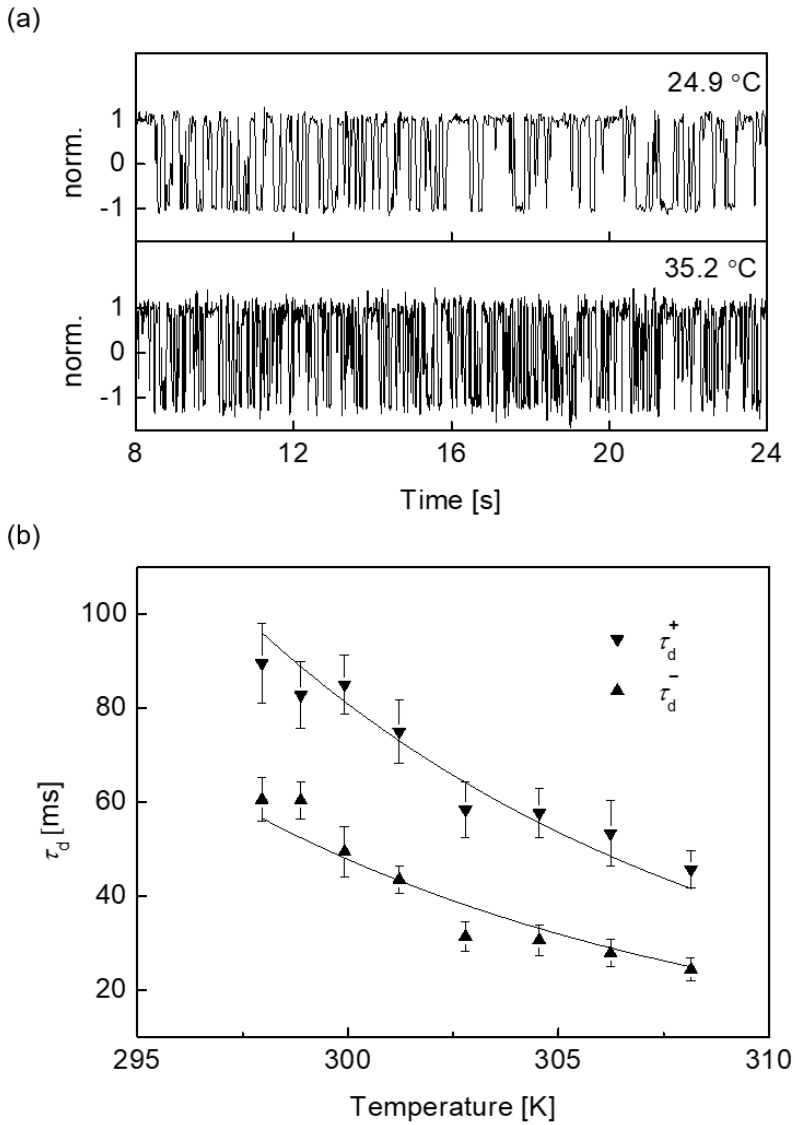


Figure 4.3 Result of temperature experiment. (a) Telegraph noise data of different temperature. (b) Plot of τ_d^\pm with respect to temperature.

in figure 3.5 (~10 min). Moreover, contrary to the temperature experiment, each measurement sequences in chapter 3 are disconnected by ~ 40 min, which has advantages to the fluctuation caused by unknown environmental effect. Another possibility is that the relaxation time before the measurement is not enough.

Because temperature of RTD equalizes exponentially in time, temperature moves very slowly after reaching a plateau in figure 4.2. In this measurement, difference of temperature relaxation between the RTD and sample substrate is overlooked. RTD is designed to conduct heat well but, sample substrate has ~ 100 nm oxidation gap which may cause dilation of heat conduction. Take points at 303 K in figure 4.3 (b) for example, those point are measured after ~ 1 hr because of refocusing and repositioning of the setup, which is quite long time compared to other points especially for the two measurement at ~ 299 and 300 K which take only few ~ 5 min before measurement. Points at 303 K both shows significant fall off which might happened when the temperature fully increased with respect to other cases. This issue can be addressed by sandwiching something between the RTD and sample stage to reduce the conducting time or take long enough time for temperature relaxation. Enlarging the temperature range by more than 2 or 3 times also can help to erase out subtleness of temperature.

In summary, by designing the add-on setup for temperature experiment, temperature dependence of the depinning rate is observed which agrees well with the Arrhenius law. It justifies the analysis of the energy barrier of domain wall depinning in which the rate of depinning is exponentially decay with rate of energy barrier to the thermal activation.

Chapter 5

Randomness of telegraph noise

In this chapter, randomness of the telegraph noise is examined. Amongst the many tests for randomness, probability and autocorrelation is checked as the basic indicator of randomness. Method to process and test the bits is presented in **Section 5.1**. Statistical concept for randomness test and corresponding test value are introduced. In **Section 5.2** and **5.3**, the defined value of probability and autocorrelation is appreciated for various field and current conditions and is determined which condition is the most random. Finally, discussion on the designing better device takes place with a summary of the chapter in **Section 5.4**.

5.1 Test method

5.1.1 Processing data to bits

Before testing the randomness, the raw data should be digitized into the bitstream of uniform sampling time. Raw data is sectioned by certain sampling time t_S and then the first data in the section is selected as a representative. The bits can be valued as ± 1 , each of which correspond to the data from p^\pm . Most of data is directly from those of chapter 3 and additional data is obtained near the current condition with fine current steps where both t_d^\pm occupy almost the same time. As mentioned in the method section in chapter 3, one set of data is obtained during the ~ 30 s which corresponds to the number of the bits from ~ 120 to ~ 12 with respect to the sampling time. As the current condition goes to the end so that the occupation t_d^\pm goes biased, the number of bits becomes half so that it is hard to make good statistics for all conditions. For this reason, the data sets of the same conditions are concatenated so the length of bits is ~ 10 min for the chapter 3 data and ~ 20 min for that of additional measurement. Time gap of each data set is ~ 40 min.

5.1.2 Definitions of test parameters

Probability P

Unpredictability is representative word which explains randomness. If the bits are unpredictable, then probability of occurrence of each bit should be equally probable. Bits becomes predictable if its occurrence favors one more than the other bit. In this thesis work, value P is defined to test the probability of occurrence of bits as follow,

$$P = \frac{1}{N} \sum_{i=1}^N x_i, \quad x_i = \pm 1 \quad (12)$$

where x_i is value of sampled bit and N is number of total bits. P ranges from -1 to $+1$ and it converges to 0 as ± 1 arise equally.

P can be rewritten in terms of time as $P = (T^+ - T^-)/(T^+ + T^-)$ where T^\pm represent total time of each bit. For large number of samples, P can be interpreted in terms of time constant τ_d^\pm as $P = (\tau_d^+ - \tau_d^-)/(\tau_d^+ + \tau_d^-)$ in that τ_d^\pm converges to average time of each state. Using equation (3) of energy barrier in chapter 3 with the assumption $\varepsilon^+ = \varepsilon^- = \varepsilon$, P can be rewritten in terms of energy barrier of pinning sites p^\pm as follow,

$$P = \tanh\left[\frac{a^+ - a^-}{2k_B T} (H^* - H_{dE_0}^*)\right] \quad (13)$$

where H^* is effective field $H^* = H - \varepsilon J$ and $H_{dE_B=0}^*$ is that which satisfies $E_B^+(H_{dE_B=0}^*) = E_B^-(H_{dE_B=0}^*)$. In this relationship, $P = 0$ is expected at $H_{dE_B=0}^*$ where two energy barriers become equivalent.

Autocorrelation R_L

The concept of probability of single bit occurrence only concerns overall statistics of total samples, which couldn't describe occurrence of bit at certain point in time. Take two of $N = 14$ bits for example, 1111-1-1-1-11111-1-1 and 1-11-11-11-11-11-11-1 are both $P = 0$ but there seems to be certain rule exist for a series of bits. Like this, no matter how equally probable the occurrence of two bits, it is predictable enough if the same bit occurs repeatedly or different bits oscillate too frequently. To check the relation between the consecutive bits, autocorrelation of the bits is investigated. In this study, autocorrelation is defined as follows,

$$R_{xx}(l) = \frac{1}{N} \sum_{i=1}^N x_i x_{i+l}, \quad x_i = \pm 1 \quad (14)$$

where l is integer which represents interval of consecutive pairs usually called 'lag'. $R_{xx}(l)$ goes to ± 1 as the same/different bits emerge repeatedly for each $l + i^{\text{th}}$ bit. Therefore, $R_{xx}(l)$ goes to 0 as x_i and x_{i+l} has little correlation. By definition $R_{xx}(0) = 1$, it is ignored for $l = 0$ and focused for $l > 0$. Unlike the representative value of probability P , equation above is function of l . To make the representative value of bits which is related to the autocorrelation function, $R_{xx}(l)$ is averaged by l as follows,

$$R_L = \frac{1}{L} \sum_{l=1}^L R_{xx}(l) \quad (15)$$

where L is integer of average range.

5.1.3 Determination of randomness

The final goal of this study is to determine whether the bits generated by the telegraph noise of domain wall motion are random or not. Random number is namely random, so all possible cases of bits have equally probable. For example, total number $N = 14$ bits of 11-1-111-1-11-11-11-1 or 111111111111-1-1 both have equal probability of occurrence $1/2^{14}$. It suggests that the randomness could not be determined by the bits themselves. However, when it comes to the statistics of the bits, it certainly has different probability for certain statistic value. Take average of bits for example, if the number is generated randomly, then the average close to 0 has higher probability than that close to 1 or -1. It is theoretically expected that the probability distribution goes to normal whose mean and standard deviation are 0 and \sqrt{N} [43]. Besides the average, it is well known by theoretical studies that several other statistics of bits have certain mathematical form of probabilistic distribution [44].

It should be noted that the discussion on theoretical probability distribution above is correct based on hypothesis of randomness where occurrence of each bit is equally probable and independent of any variables for example, time, previous or next bit, frequency, etc. In this study, hypothesis test is adopted which is generally conducted to examine the randomness of bits [44].

Figure 5.1 shows example of probability distribution of one fictional test statistic which is expected to have normal distribution. It shows that values at the center is most likely to happen and the values at tails have less likely to happen. One can easily calculate the probability of a test value less probable than a particular value coming out by integrating both tails whose area is below the probability of the certain value. In the hypothesis test, limitation of probability of unlikely statistic coming out, which is called level of significance α , is set to a certain value then, a critical value is determined by the boundary which discriminates the area containing the level of significance from the other. If the test statistic comes out to be inside the critical value, then hypothesis of randomness is accepted and if it is out of the critical value then, the hypothesis was rejected as it was considered a significant result. Level of significant α is usually 0.01 or 0.05 (or it can be written in % unit like 1% or 5%) for the random number test [44]. It should be noted that tests can have single critical value by

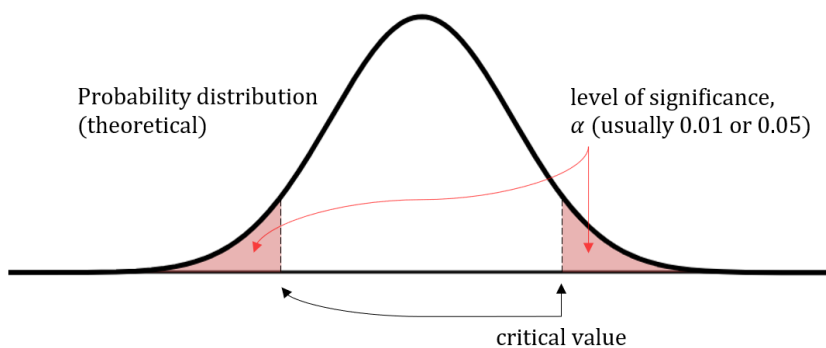


Figure 5.1 Conceptual description of hypothesis test.

defining test value having half normal distribution. The figure above is described for the convenience of explanation. The theoretical distribution is dependent on the test statistics, not all the test statistics have normal distribution. However, in this thesis work, we consider only two test statistics which is expected to be normal distribution.

Instead of determining randomness by critical value, randomness test usually calculates so called p -value, the probability of the random generator generating the test statistic which is equal or more unlikely to the test result assuming the hypothesis of randomness. It can be thought as integrating tails from test result. The p -value is directly compared to the level of significance α so if the p -value is over α then the hypothesis accepted.

5.2 Probability of telegraph noise

5.2.1 Control of probability P

Figure 5.2 (a) plots the probability P defined as equation the bits of which is sampled from the experiment of figure 3.5. For each field conditions, P varies from 1 to -1 as current increases. Each plot is fitted in hyperbolic tangent lines of equation which show high accuracy for all plots, reinforcing again the equality assumption of spin-torque efficiency, $\varepsilon^+ = \varepsilon^- = \varepsilon$. The result of field zero in the figure suggests that the P can be solely controlled by the current which is important factor for device applications.

According to the fitting equation, effective field of $P = 0$, $H_{P=0}^*$, should be the same with $H_{dE_B=0}^*$. To verify this, $H_{dE_B=0}^*$ is obtained by fitting the data of $dE_B = E_B^+ - E_B^-$ for each field condition. Result is plotted in figure 5.2 (b). Points obtained by $H_{dE_B=0}^*$ (black square) and $H_{P=0}^*$ (red circle) coincide with each other, suggesting that the random bits result from which the energy barriers of each pinning sites are equal. And the fitting lines of $H_{dE_B=0}^*$ implies that $H_{P=0}^*$ condition can be applied to the point which lies on the fitting line. Spin-torque efficiency ε obtained by this fitting is $9.7 \pm 0.2 \cdot 10^{-14} \text{ Am}^{-2}$ which is well matched with the results from the table I.

5.2.2 Randomness determination of P

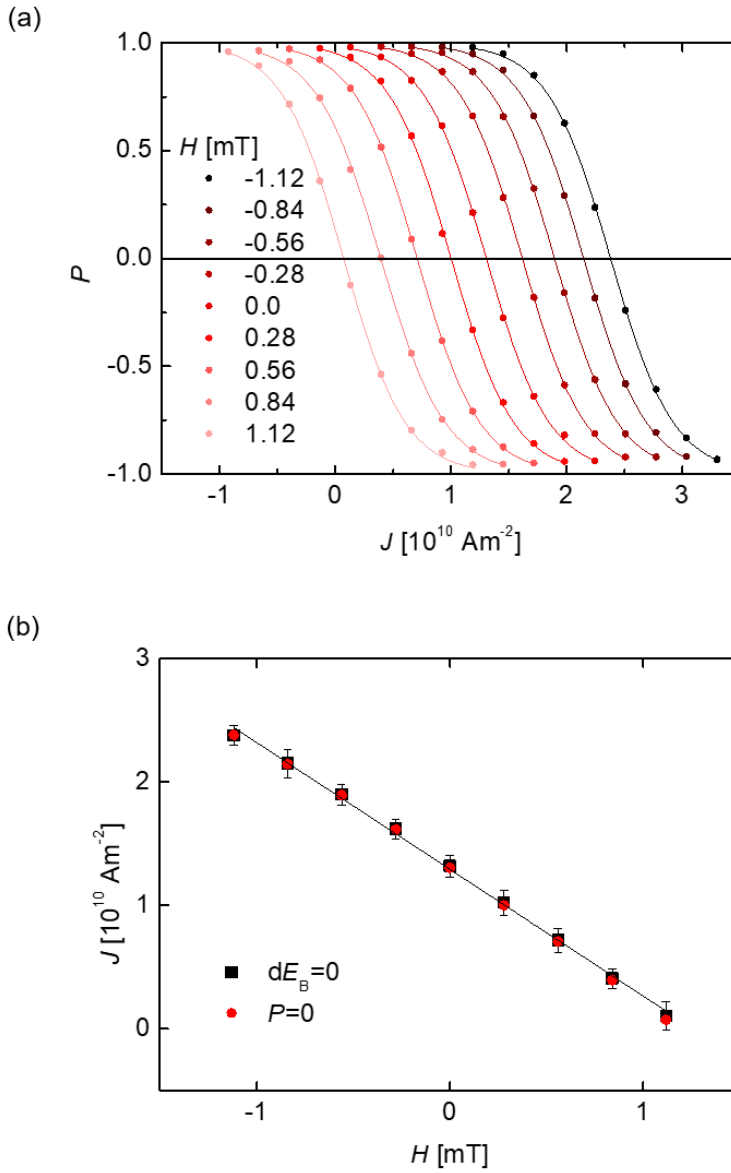


Figure 5.2 Controllability test result of probability of bit. (a) Current density vs P . (b) $H_{dE_B=0}^*$ (black) and $H_{P=0}^*$ (red) with respect to the field.

To test the randomness of bits according to the probability, definition of the P is revised to adequate for the test. According to the central limit

theorem [43,44], $P\sqrt{N}$ approximates to the normal distribution. In the reference 44 about the test for random number generator, it defines test statistics to take the absolute value, $|P|\sqrt{N}$ and then determine the randomness by p -value which is calculated by the equation as follow

$$p\text{-value} = \text{erfc}\left(\frac{|P|\sqrt{N}}{\sqrt{2}}\right) \quad (16)$$

where erfc is complementary error function.

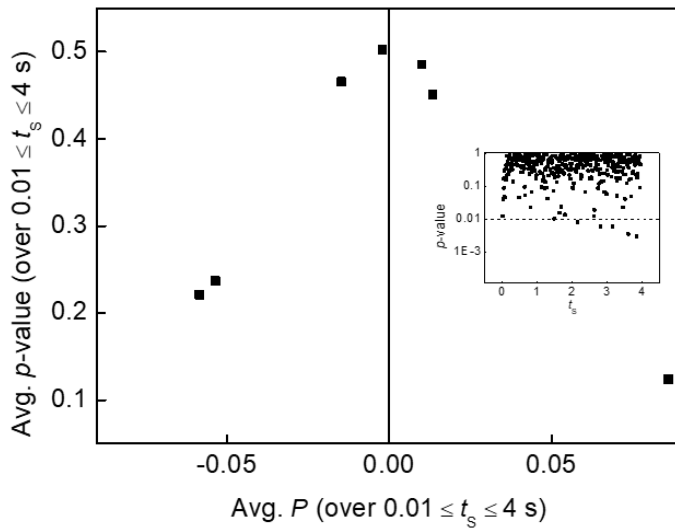


Figure 5.3 Randomness test for probability of bit. Inset shows **p -values** for each sampling rate

Figure 5.3 shows the results acquired from the p -value of the bits which is sampled by time variable t_s from 0.01 to 4 seconds. The data is obtained by the 7 effective field conditions where it results in P close to 0. Each point in the plot is obtained by averaging all p -value over every sampling

time variation. As seen in the graph, the closer averaged P is to the zero, the higher averaged p -value is, which means that the random number generator behaves more randomly in average. It should be noted that the random number test is targeted only single p -value obtained single bits. The inset of the graph shows the p -value of the bits of the highest point of the averaged with respect to the t_5 . Dashed line indicates 0.01 which is level of significance of the test [44]. The sampled bits are found out to be random except for the 6 points. It can be concluded that randomness of bits according to the probability of bits occurrence can be controlled by the current variation.

5.3 Autocorrelation of telegraph noise

5.3.1 Properties of autocorrelation

Autocorrelation function $R_{xx}(l)$ is function of lag l which is interval of tested pairs. For truly random bits the $R_{xx}(l)$ should be constant zero for all l . If the bits are sampled so fast that the sampling time is much smaller than average oscillating period of bits, however, then it easily expected that a number of consecutive same bits may arise. This situation is well described in figure 5.4 (a) which plots $R_{xx}(l)$ of the bits. The data of the bits are of the inset of figure 5.3 (b) that shows highest randomness in probability of bits occurrence. Plots shows high correlation at low l , which goes significant as sampling time t_s decreases. Decaying constant of each plot can be obtained by exponential fitting, which results in ~ 64 ms for all fitted data (black, red and green plots). Only over the few hundred ms of t_s the $R_{xx}(l)$ shows no correlation (blue plot). To increase the t_s can zero the correlation of bits, which decreases the performance of bit generating rate. So, criterion is needed to select minimum t_s which keeps bits random.

To test the randomness and select proper t_s , testing $R_{xx}(1)$ is sufficient for examine full autocorrelation. Runs test [45] is well-known random test corresponds to $R_{xx}(1)$. The word ‘run’ means the set of consecutive same bits and the test determines whether the test value of runs is

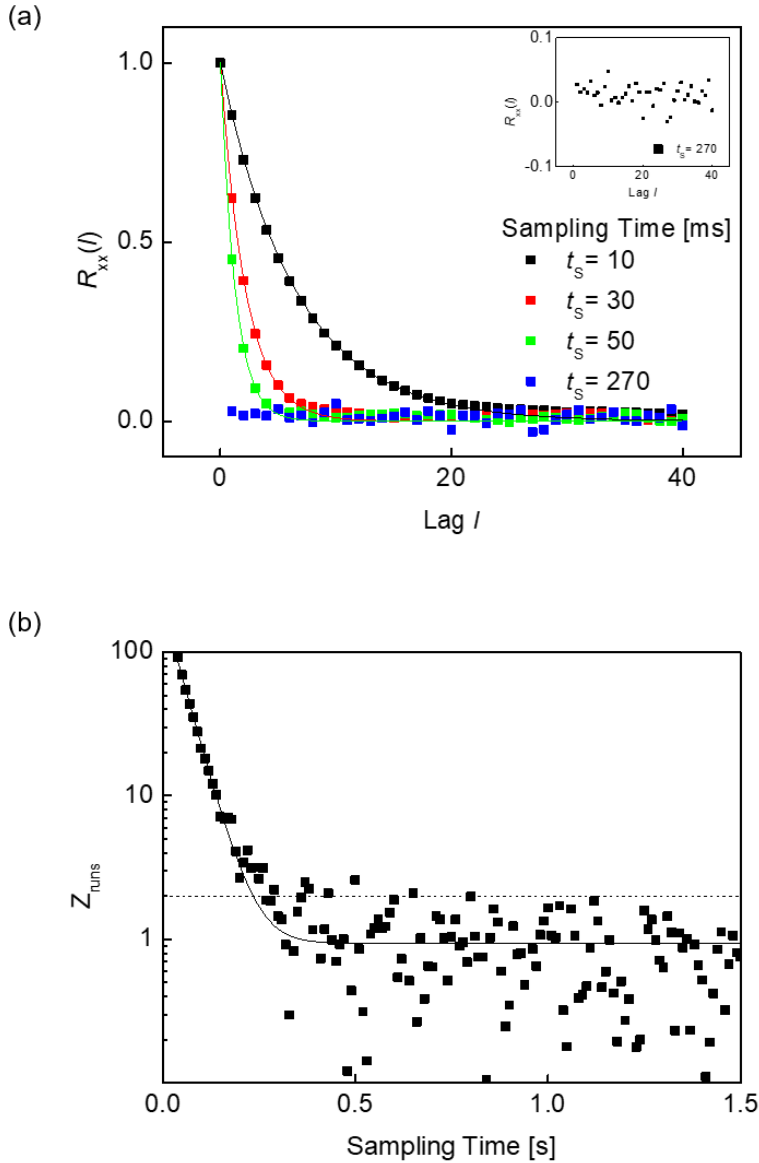


Figure 5.4 Properties of $R_{xx}(l)$ with respect to the sampling time t_s . (a) Lag l vs $R_{xx}(l)$ in different t_s s. (b) Result of runs test related to $R_{xx}(l = 1)$ in different t_s s.

well under the critical value when the numbers of each bit N^\pm is given. Take bits of $N^\pm = 5$ for example, detailed sequence could be 11111-1-1-1-1-1,

1-11-11-11-11-1, the number of runs of which is 2 and 10 each. In the hypothesis of randomness, two of example both are at the extreme. Theoretically, the probability of runs has normal distribution whose expected mean and standard deviation of runs are as follows,

$$\begin{cases} \mu = \frac{2N^+N^-}{N^+ + N^-} + 1 & \text{(mean)} \\ \sigma^2 = \frac{2N^+N^-(2N^+N^- - N^+ - N^-)}{(N^+ + N^-)^2(N^+ + N^- + 1)} & \text{(var.)} \end{cases} \quad (17)$$

for large number of total bits. Test statistic and criterion of randomness for the runs are as follows,

$$\begin{cases} Z_{\text{runs}} = \frac{R - \mu}{\sigma} \\ |Z_{\text{runs}}| > 1.96 \end{cases} \quad (18)$$

where the R is the number of runs and 1.96 is the critical value of the test statistic which is related to the level of significance $\alpha = 0.05$. The result is plotted on figure 5.4 (b). $|Z_{\text{runs}}|$ of bits is calculated for several sampling times from 0.01 to 4 s. It decays exponentially and bounds in random conditions for $t_s \geq \sim 270$ ms. With this graph, we can determine the smallest sampling time for random bits. The inset in figure 5.3 (a) shows $R_{xx}(l)$ of bits sampled by $t_s = 270$ ms zoomed in near the zero. It shows no correlation in l over 0 to 40.

5.3.2 Control of probability R_L

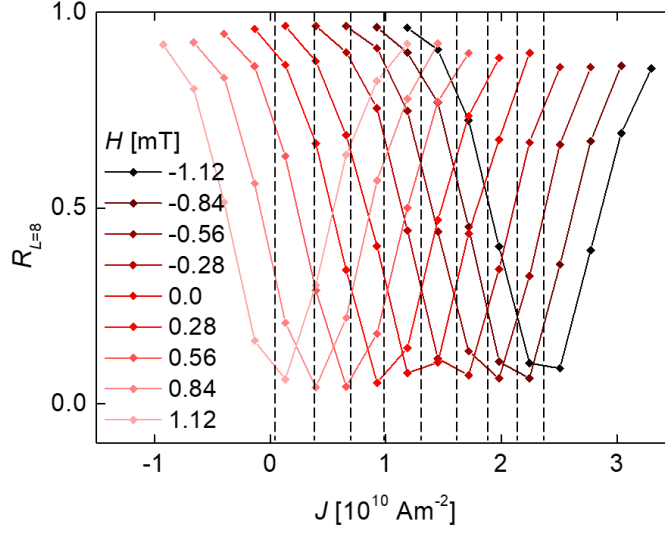


Figure 5.5 Controllability test of R_L with respect to current. Dashed line is $H_{dE_B=0}^*$ from figure 5.2 (b).

Dependence of autocorrelation on current is to be tested by the test value R_L defined in section 5.1 which averages the $R_{xx}(l)$ over lag L . In this test, L is set to 8 because it forms the unit byte. The dataset of the bits is the same as that of figure 3.5 and hence of figure 5.2 (b). Using the results of the minimum sampling time, all data are sampled by 270 ms. Result is plotted on the figure 5.5. For all field conditions, R_L behaves identically with respect to the applied current. It minimizes near each dashed line which is the indicator of $H_{P=0}^*$ (or $H_{dE=0}^*$). This result suggests that the condition for randomness is the same for P and R_L , which is good news for device applications because it need not compensate for any randomness properties.

5.4 Summary with comments on device applications

For the conclusion of the chapter, considerations for device application of random number generator are discussed. According to the results of section 5.2 and 5.3, it is possible enough to control the randomness of telegraph noise by applied current. Although there are the other randomness tests not covered in this thesis, both two tests in the previous section are considered the priority properties by the reference 44. Therefore, it can be said that the two tests are for examining the basic viability of device applications. Testing all the randomness properties in the reference will be meaningful when the domain wall telegraph noise system is equipped to function as independent number generator, without the aid of PC and heavy measurement system, like other studies of true random number generator did [13,46,47]. The first step for independent device may be to develop electrical measurement method.

One of the important factors in determining the good device is the sampling rate of the random number. According to the results of previous section, autocorrelation limits the sampling time. To lower the limit, oscillation of telegraph noise occurs much frequently. To analyze the frequency of the randomly oscillating noise, $\tau_{\text{osc}} := \tau^+ + \tau^-$ is defined for a representative of oscillating period, which converges to average period for large number of bits. With the variables defined in this paper, H_{fast}^* , effective field that minimize τ_{osc} , can be derived by differentiation. Result of calculating $\frac{d\tau_{\text{osc}}}{dH^*}(H_{\text{fast}}^*) = 0$

is as follows.

$$H_{\text{fast}}^* = H_{dE=0}^* - \frac{1}{d\tilde{a}} \ln \left(-\frac{a^+}{a^-} \right) \quad (19)$$

where $d\tilde{a} = (a^+ - a^-)/k_B T$ and the assumption $\varepsilon = \varepsilon^+ = \varepsilon^-$ is used again. From the discussion in chapter 3, signs of a^\pm are always opposite so, the $d\tilde{a} \neq 0$ and value $-a^+/a^-$ in logarithm is always positive. It is also checked that the calculated value is minimum by the result of $\frac{d^2\tau_{\text{osc}}}{dH^{*2}} > 0$. It is noticeable that H_{fast}^* is slightly different from the $H_{dE=0}^*$ in which the probability and autocorrelation becomes zero. This is systematic disadvantage for the real applications. Condition for $H_{\text{fast}}^* = H_{dE=0}^*$ is $|a^+| = |a^-|$, which is directly related to the length of each pinning sites according to the analytic derivation of the energy barrier.

To develop the device utilizing pinning of domain wall, pinning site should be fabricated artificially by means of electron beam, Ga⁺ ion damaging [33], or etc. Especially for the e-beam, as the resolution is ten few nanometers, it can be used for realizing the size similar to that obtained in chapter 3. As one candidate for the origin of domain wall pinning is the magnetic vacancy [40], it is expected that the pinning site is made by damaging with e-beam. Condition $H_{\text{fast}}^* = H_{dE=0}^*$ can be realized simply by fabricating two identical pinning sites. Moreover, if the correlation between a and E_0 really exists as discussed in chapter 3, then the condition $H_{\text{fast}}^* = H_{dE=0}^*$ makes both E_0^\pm similar to each other, which would make $H_{\text{fast}}^* \simeq 0$ meaning zero

energy consumption.

Direct method to decrease the τ_{osc} is to manipulate the depinning rate which is related to the Arrhenius law. According to the law, there is two possible ways to increase the depinning rate, 1) lowering both energy barriers E_0^\pm or 2) increasing the base temperature. First one can be included in the previous paragraph of artificial depinning site. Easier method would be to increase the temperature of the system. As seen in the chapter 4, τ^\pm decrease to the half by 10 °C increment. Temperature control would be realized in device with additional isolated current lines for joule heating.

Although every measurement of telegraph noise in this thesis study is done optically, electric measurements should be adopted for the device implementation. Hall bar structure can be the solution for the electric measurement. Contrary to the optical measurements, telegraph noise can be measured in parallel in electrical measurements scheme, which can speed up the effective rate of random number generation.

Summary

Randomness of the telegraph noise is tested for two properties, probabilities and autocorrelation of bit occurrence. P , a property related to the probabilities, follows clear hyperbolic tangent line with respect to current as expected by analysis on the energy barrier. It is shown that higher randomness

of P can be achieved by fine tuning the current application. Bits shows higher correlation as compared pair is closer, or lag l is lower, which gets worse as the sampling time is shorter. Minimum sampling time is decided to 0.27 s by runs test related to $R_{xx}(0)$. Condition for minimum of $R_{L=8}$, average of $R_{xx}(l)$ over $l = 1 \dots 8$ which represent randomness related to autocorrelation, is found to be identical to the condition of P . With the analysis on energy barrier, ideas for device design are developed which can be realized by extended study on developing method to fabricate artificial pinning site.

Chapter 6

Conclusion

In this thesis, domain wall dynamics generating telegraph noise is elucidated by investigating energy landscape of the system in various field and current condition. To verify the phenomena, experimental system with high spatial resolution and low noise is developed, which is optimized to measure minute motion of domain wall. Sample of the experiment is selected and fabricated with care which is fit to the measurement of telegraph noise. With the effort above, it is clearly shown that the system generating telegraph noise has single energy barrier which follows the Arrhenius law. Furthermore, the telegraph noise shows clear linear dependence on applied magnetic field and electric current, which show potential to be used for device application. Analytic calculation for deriving formula of energy barrier has been done with 1-D collective model of domain wall motion under spin-orbit torque and Dzyaloshinskii-Moriya interaction and, the linear dependency is derived with the parameter associated with the size of the telegraph noise system and each pinning site. The distance between pinning sites of telegraph noise sites estimated from the analytics is compared with the estimates by optical signal level of telegraph noise, which fits to the expected values in order of few nanometer.

To supplement the study of energy barrier, Arrhenius law is verified by temperature experiment of time constant τ of telegraph noise. By designing the add-on setup, which is optimized for temperature experiment, τ decreases following the curve of Arrhenius law, which justifies the assumption of energy barrier in Chapter 3.

Possibilities of device implementation is also tested by examine the randomness of the bits sampled by telegraph noise. Raw data is sectioned with certain sampling rate and converted to the bits 1 and -1. Probability defined in the thesis work shows that it goes to zero, or equiprobable, when the difference of the energy barriers of the two pinning sites are zero, which is reasonable result and show controllability of bit occurring probabilities. Autocorrelation of the bits is also examined which related to the predictabilities of right next or l^{th} next bit of the random numbers. It is shown that the sampling time is related to the autocorrelation so, the sampling time is decided by testing autocorrelation of right next bit. With proper sampling time, the average value of autocorrelation over testing integer l goes to zero when the bits go to equiprobable state. With combining testing result with the analytic formula of the energy barrier, some consideration for designing device is also suggested which is promising for realization of true random number generator using domain wall motion.

References

- [1] A. van der Ziel and E. R. Chenette, *Noise in Solid State Devices*, in *Advances in Electronics and Electron Physics*, edited by L. Marton, Vol. 46 (Academic Press, 1978), pp. 313–383.
- [2] M. J. Kirton and M. J. Uren, *Noise in Solid-State Microstructures: A New Perspective on Individual Defects, Interface States and Low-Frequency ($1/f$) Noise*, *Advances in Physics* **38**, 367 (1989).
- [3] R. J. Roedel and C. R. Viswanathan, *Reduction of Popcorn Noise in Integrated Circuits*, *IEEE Transactions on Electron Devices* **22**, 962 (1975).
- [4] C. Leyris, F. Martinez, M. Valenza, A. Hoffmann, J. C. Vildeuil, and F. Roy, *Impact of Random Telegraph Signal in CMOS Image Sensors for Low-Light Levels*, 2006 Proceedings of the 32nd European Solid-State Circuits Conference 376 (2006).
- [5] K. Abe, A. Teramoto, S. Sugawa, and T. Ohmi, *Understanding of Traps Causing Random Telegraph Noise Based on Experimentally Extracted Time Constants and Amplitude*, in *2011 International Reliability Physics Symposium* (2011), pp. 4A.4.1-4A.4.6.
- [6] S. Choi, Y. Yang, and W. Lu, *Random Telegraph Noise and Resistance Switching Analysis of Oxide Based Resistive Memory*, *Nanoscale* **6**, 400 (2014).
- [7] E. A. Montoya, S. Perna, Y.-J. Chen, J. A. Katine, M. d’Aquino, C. Serpico, and I. N. Krivorotov, *Magnetization Reversal Driven by Low Dimensional Chaos in a Nanoscale Ferromagnet*, *Nature Communications* **10**, 543 (2019).
- [8] J. Cucchiara, Y. Henry, D. Ravelosona, D. Lacour, E. E. Fullerton, J. A. Katine, and S. Mangin, *Telegraph Noise Due to Domain Wall Motion*

- Driven by Spin Current in Perpendicular Magnetized Nanopillars*, Applied Physics Letters **94**, 102503 (2009).
- [9] G. Yang, D. Kim, J. W. Yang, S. Barraud, L. Brevard, G. Ghibaudo, and J. W. Lee, *Reduction of Random Telegraph Noise by High-Pressure Deuterium Annealing for p-Type Omega-Gate Nanowire FET*, Nanotechnology **31**, 415201 (2020).
- [10] L. Thomas et al., *Perpendicular Spin Transfer Torque Magnetic Random Access Memories with High Spin Torque Efficiency and Thermal Stability for Embedded Applications (Invited)*, Journal of Applied Physics **115**, 172615 (2014).
- [11] B. Jun and P. Kocher, THE INTEL ® RANDOM NUMBER GENERATOR CRYPTOGRAPHY RESEARCH, INC. WHITE PAPER PREPARED FOR INTEL CORPORATION, 1999.
- [12] L. Gong, J. Zhang, H. Liu, L. Sang, and Y. Wang, *True Random Number Generators Using Electrical Noise*, IEEE Access **7**, 125796 (2019).
- [13] J. Brown, J. F. Zhang, B. Zhou, M. Mehedi, P. Freitas, J. Marsland, and Z. Ji, *Random-Telegraph-Noise-Enabled True Random Number Generator for Hardware Security*, Scientific Reports **10**, 17210 (2020).
- [14] S. Kanai, K. Hayakawa, H. Ohno, and S. Fukami, *Theory of Relaxation Time of Stochastic Nanomagnets*, Physical Review B **103**, 94423 (2021).
- [15] S. S. P. Parkin, M. Hayashi, and L. Thomas, *Magnetic Domain-Wall Racetrack Memory*, Science (1979) **320**, 190 (2008).
- [16] J. P. Attané, D. Ravelosona, A. Marty, Y. Samson, and C. Chappert, *Thermally Activated Depinning of a Narrow Domain Wall from a Single Defect*, Physical Review Letters **96**, 147204 (2006).
- [17] K.-J. Kim, J. Ryu, G.-H. Gim, J.-C. Lee, K.-H. Shin, H.-W. Lee, and S.-B. Choe, *Electric Current Effect on the Energy Barrier of Magnetic Domain Wall Depinning: Origin of the Quadratic Contribution*, Physical Review Letters **107**, 217205 (2011).

- [18] V. D. Nguyen, W. S. Torres, P. Laczowski, A. Marty, M. Jamet, C. Beigné, L. Notin, L. Vila, and J. P. Attané, *Elementary Depinning Processes of Magnetic Domain Walls under Fields and Currents*, *Scientific Reports* **4**, 6509 (2014).
- [19] S.-J. Yun, S.-C. Yoo, S.-B. Choe, and B.-C. Min, *Determination of the Energy Barrier and Spin Torque Efficiency Based on Telegraph Noise*, *Journal of the Korean Physical Society* **65**, 1607 (2014).
- [20] J. Ryu, S.-B. Choe, and H.-W. Lee, *Magnetic Domain-Wall Motion in a Nanowire: Depinning and Creep*, *Physical Review B* **84**, 75469 (2011).
- [21] C. Garg, A. Pushp, S.-H. Yang, T. Phung, B. P. Hughes, C. Rettner, and S. S. P. Parkin, *Highly Asymmetric Chiral Domain-Wall Velocities in Y-Shaped Junctions*, *Nano Letters* **18**, 1826 (2018).
- [22] L. Thomas, R. Moriya, C. Rettner, and S. S. P. Parkin, *Dynamics of Magnetic Domain Walls Under Their Own Inertia*, *Science* (1979) **330**, 1810 (2010).
- [23] J. Wunderlich, D. Ravelosona, C. Chappert, F. Cayssol, V. Mathet, J. Ferre, J.-. Jamet, and A. Thiaville, *Influence of Geometry on Domain Wall Propagation in a Mesoscopic Wire*, *IEEE Transactions on Magnetics* **37**, 2104 (2001).
- [24] Y.-K. Park, J.-S. Kim, Y.-S. Nam, S. Jeon, J.-H. Park, K.-W. Kim, H.-W. Lee, B.-C. Min, and S.-B. Choe, *Interfacial Atomic Layers for Full Emergence of Interfacial Dzyaloshinskii–Moriya Interaction*, *NPG Asia Materials* **12**, 38 (2020).
- [25] X. Zhang, J. Mao, M. Chang, Z. Yan, Y. Zuo, and L. Xi, *Current-Induced Magnetization Switching in Pt/Co/W and Pt/Co/W_{0.82}Pt_{0.18} Structures with Perpendicular Magnetic Anisotropy*, *Journal of Physics D: Applied Physics* **53**, 225003 (2020).
- [26] K. J. Kim and S. B. Choe, *Analytic Theory of Wall Configuration and Depinning Mechanism in Magnetic Nanostructure with Perpendicular*

- Magnetic Anisotropy*, Journal of Magnetism and Magnetic Materials **321**, 2197 (2009).
- [27] E. Saitoh, H. Miyajima, T. Yamaoka, and G. Tatara, *Current-Induced Resonance and Mass Determination of a Single Magnetic Domain Wall*, Nature **432**, 203 (2004).
- [28] A. Thiaville, S. Rohart, É. Jué, V. Cros, and A. Fert, *Dynamics of Dzyaloshinskii Domain Walls in Ultrathin Magnetic Films*, EPL (Europhysics Letters) **100**, 57002 (2012).
- [29] S. Rohart and A. Thiaville, *Skyrmion Confinement in Ultrathin Film Nanostructures in the Presence of Dzyaloshinskii-Moriya Interaction*, Physical Review B **88**, 184422 (2013).
- [30] S.-G. Je, D.-H. Kim, S.-C. Yoo, B.-C. Min, K.-J. Lee, and S.-B. Choe, *Asymmetric Magnetic Domain-Wall Motion by the Dzyaloshinskii-Moriya Interaction*, Physical Review B **88**, 214401 (2013).
- [31] D.-Y. Kim, D.-H. Kim, J. Moon, and S.-B. Choe, *Determination of Magnetic Domain-Wall Types Using Dzyaloshinskii-Moriya-Interaction-Induced Domain Patterns*, Applied Physics Letters **106**, 262403 (2015).
- [32] S. Emori, U. Bauer, S.-M. Ahn, E. Martinez, and G. S. D. Beach, *Current-Driven Dynamics of Chiral Ferromagnetic Domain Walls*, Nature Materials **12**, 611 (2013).
- [33] P. P. J. Haazen, E. Murè, J. H. Franken, R. Lavrijsen, H. J. M. Swagten, and B. Koopmans, *Domain Wall Depinning Governed by the Spin Hall Effect*, Nature Materials **12**, 299 (2013).
- [34] S.-G. Je, S.-C. Yoo, J.-S. Kim, Y.-K. Park, M.-H. Park, J. Moon, B.-C. Min, and S.-B. Choe, *Emergence of Huge Negative Spin-Transfer Torque in Atomically Thin Co Layers*, Physical Review Letters **118**, 167205 (2017).
- [35] J. F. C. (John F. C. Kingman, *Poisson Processes*, Poisson processes /

- J.F.C. Kingman.
- [36] D. Ravelosona, D. Lacour, J. A. Katine, B. D. Terris, and C. Chappert, *Nanometer Scale Observation of High Efficiency Thermally Assisted Current-Driven Domain Wall Depinning*, *Physical Review Letters* **95**, 117203 (2005).
- [37] K.-J. Kim et al., *Two-Barrier Stability That Allows Low-Power Operation in Current-Induced Domain-Wall Motion*, *Nature Communications* **4**, 2011 (2013).
- [38] T. Yomogita, S. Okamoto, N. Kikuchi, O. Kitakami, H. Sepehri-Amin, Y. K. Takahashi, T. Ohkubo, K. Hono, K. Hioki, and A. Hattori, *Direct Detection and Stochastic Analysis on Thermally Activated Domain-Wall Depinning Events in Micropatterned Nd-Fe-B Hot-Deformed Magnets*, *Acta Materialia* **201**, 7 (2020).
- [39] Y.-K. Park, J.-S. Kim, Y.-S. Nam, S. Jeon, J.-H. Park, K.-W. Kim, H.-W. Lee, B.-C. Min, and S.-B. Choe, *Interfacial Atomic Layers for Full Emergence of Interfacial Dzyaloshinskii–Moriya Interaction*, *NPG Asia Materials* **12**, 38 (2020).
- [40] S. Chikazumi, *Physics of Ferromagnetism / Sōshin Chikazumi ; English Edition Prepared with the Assistance of C.D. Graham, Jr*.
- [41] J. Yoon, S.-W. Lee, J. H. Kwon, J. M. Lee, J. Son, X. Qiu, K.-J. Lee, and H. Yang, *Anomalous Spin-Orbit Torque Switching Due to Field-like Torque–Assisted Domain Wall Reflection*, *Science Advances* **3**, e1603099 (2022).
- [42] G. E. W. Bauer, E. Saitoh, and B. J. van Wees, *Spin Caloritronics*, *Nature Materials* **11**, 391 (2012).
- [43] O. C. (Oliver C. Ibe, *Fundamentals of Applied Probability and Random Processes*, *Fundamentals of applied probability and random processes / Oliver Ibe*.
- [44] L. E. Bassham et al., *A Statistical Test Suite for Random and*

Pseudorandom Number Generators for Cryptographic Applications, 2010.

- [45] J. V. (James V. Bradley, *Distribution-Free Statistical Test / James V. Bradley*.
- [46] H. Jiang et al., *A Novel True Random Number Generator Based on a Stochastic Diffusive Memristor*, Nature Communications **8**, 882 (2017).
- [47] G. Kim, J. H. In, Y. S. Kim, H. Rhee, W. Park, H. Song, J. Park, and K. M. Kim, *Self-Clocking Fast and Variation Tolerant True Random Number Generator Based on a Stochastic Mott Memristor*, Nature Communications **12**, 2906 (2021).

Abstract in Korean

국문 초록

현대 사회에서는 많은 정보, 특히 계좌번호와 같은 1 개인정보가 디지털 데이터화 되고 있다. 이에 따라 데이터의 암호화에 대한 관심이 높아지고 있는 상황이다. 많은 경우에 컴퓨터 알고리즘을 통해 암호화를 하지만, 이러한 암호화 방식은 일반적으로 고유 입력 값, 즉 '시드(Seed) 값'이 필요하다. 이러한 시드 값은 어떠한 알고리즘으로도 예측할 수 없어야 하므로 소프트웨어를 이용한 생성은 고려대상이 되지 않는다. 따라서 주사위를 굴리거나 동전을 던지는 것과 같은 하드웨어를 사용하는 난수가 필요하다. 이러한 난수 생성을 칩셋과 같은 소형 디바이스로 구현한 것을 진정한 난수 발생기(True Random Number Generator) 또는 하드웨어 난수 발생기(Hardware Random Number Generator)라고 한다.

진정한 난수 발생기를 설계하려면 난수의 소스를 선택하는 것이 중요하다. 진정한 난수 발생기에 대한 여러 연구들은 좋은 난수 발생기에 적합한 소스를 찾고 적용하는 데 중점을 둔다. 이를 만족시키는 후보들 중 하나는 2 레벨 디지털 비트와 유사한 텔레그래프 노이즈(Telegraph Noise)이다. 이 학위논문은 자구벽

운동으로 생성되는 텔레그래프 노이즈를 이해하고 자구벽의 에너지 장벽에 대한 이해를 활용하여 장치의 응용 및 테스트에 초점을 두었다.

그 첫 번째 단계로 텔레그래프 노이즈 측정 시스템을 개발하고 이에 적절한 자성 박막 샘플을 제작하였다. 텔레그래프 노이즈 감지에 특화된 자기광 커 효과 현미경(Magneto-Optic Kerr Effect Microscope)이 개발되었으며, 자기장 및 전류인가 자구벽 운동이 자연스럽게 이루어지는 샘플이 선택되었다. 그리고 자구벽 디피닝(depining) 현상의 제어 및 반복 가능한 측정 방법이 확립되었다.

그런 다음, 자구벽 에너지 장벽과 자기장 혹은 전류와 같은 외부 입력 사이의 관계를 규명하기 위해, 여러 자기장과 전류 조건에서의 자구벽 에너지 장벽을 이해하는 실험을 수행했다. 텔레그래프 노이즈의 디피닝 시간의 통계와 아레니우스(Arrhenius)법칙을 상정하여, 여러 조건에서의 자구벽 에너지 장벽 값을 구해냈다. 그리고 에너지 장벽의 해석적인 유도를 통해 이러한 관계의 물리적인 이해를 도모했다.

다음으로 아레니우스 법칙이 자구벽 운동에서 실제로 작동하는지 확인하였다. 이를 위해 온도 변화가 가능한 시스템이 구축되어야 했으며, 이를 구현하여 넓은 온도 범위에서 원활히 작동하는지 확인하였다. 텔레그래프 노이즈로부터 얻어진 통계치의 온도 의존성은 아레니우스 법칙을 잘 설명하는 결과를 보여주었다.

마지막으로 자구벽 텔레그래프 노이즈로부터 얻어진 난수를 테스트했다. 비트의 확률 및 자기상관과 같은 기본 테스트가 수행되었으며 진정한 랜덤 비트를 생성해내는 적절한 자기장 및 전류 조건을 찾아냈다. 가설 검정을 통한 난수 발생기의 테스트 또한 이루어졌다. 그리고 앞에서 이루어진 에너지 장벽에 대한 이해를 접목시켜, 예측 불가능하고 빠른 난수 발생기를 위한 이론적 접근을 시도하였다.

이러한 전신 노이즈를 이해하고 테스트하기 위한 연구는, 장효과 트랜지스터(Field Effect Transistor), 멤리스터 (Memristor) 또는 자기 터널 접합(Magnetic Tunnel Junction)와 같은 기존의 텔레그래프 노이즈 기반 난수 발생기 연구에서 한 발 나아가, 새로운 형태인 자구벽 기반의 진정한 난수 발생기를 개발하는 출발점이 될 것으로 기대한다.

Author's Biography

Jeon, Seyyoung

THz magnetic nanodevice Lab., 23-410, Department of Physics and Astronomy,
Seoul National Univ., Gwanakro, Shillim-dong, Gwanak-gu, Seoul, 151-747,
Korea

Phone: +82-2-884-9254 Fax: +82-2-884-9254

E-mail: seyng1990@snu.ac.kr

Education

Ph.D.† Seoul National University Mar. 2013~ Aug. 2022 Physics

B.S. Seoul National University Mar. 2008~Feb. 2013 Physics

† Advisor Choe, Sug-Bong (Condensed matter physics)

Publications

1. Manh Duc Le, **Seyyoung Jeon**, A. I. Kolesnikov, D. J. Voneshen, A. S. Gibbs, Jun Sung Kim, Jinwon Jeong, Han-Jin Noh, Changhwi Park, Jaejun Yu, T. G. Perring, and Je-Geun Park, Magnetic Interaction of PdCrO₂ and Their Effects on Its Magnetic Structures, Phys. Rev. B 98, 024429 (2018)
2. Yong-Keun Park, Joo-Sung Kim, Yune-Seok Nam, **Seyyoung Jeon**, Jung-Hyun Park, Kyoung-Whan Kim, Hyun-Woo Lee, Byoung-Chul Min & Sug-Bong Choe, Interfacial Atomic Layers for Full Emergence of Interfacial Dzyaloshinskii-Moriya interaction, NPG Asia Materials 12, 38 (2020)
3. **Seyyoung Jeon**, Seong-Hyub Lee, Sug-Bong Choe, “Energy landscape study by telegraph noise of domain wall motion”, submitted to Current Applied Physics